Expérimentations

Table des matières

Available online at www.sciencedirect.com
ScienceDirect
Geochimica et Cosmochimica Acta 73 (2009) 2693–2711
Geochimica et Cosmochimica Acta
www.elsevier.com/locate/gca

Mercury isotope fractionation during liquid–vapor evaporation experiments

Nicolas Estrade [a,b,*], Jean Carignan [a], Jeroen E. Sonke [c], Olivier F.X. Donard [b]

[a] *Centre de Recherche Pétrographique et Géochimique, Nancy Université, CNRS UPR 2300, BP 20, 54501 Vandoeuvre les Nancy, France*
[b] *Institut Pluridisciplinaire de Recherche sur l'Environnement et les Matériaux, Laboratoire de Chimie-Analytique Bio-Inorganique et Environnement, Université de Pau et des Pays de l'Adour, CNRS UMR 5254, HELIOPARC, 64053 Pau, France*
[c] *Observatoire Midi-pyrénées, Laboratoire des Mécanismes et Transferts en Géologie, CNRS/IRD/Université Toulouse 3, UMR 5563 UR 154, 14 avenue Edouard Belin, 31400 Toulouse, France*

Received 6 October 2008; accepted in revised form 16 January 2009; available online 5 February 2009

Abstract

Liquid–vapor mercury isotope fractionation was investigated under equilibrium and dynamic conditions. Equilibrium evaporation experiments were performed in a closed glass system under atmospheric pressure between 0 and 22 °C, where vapor above the liquid was sampled at chemical equilibrium. Dynamic evaporation experiments were conducted in a closed glass system under 10^{-5} bar vacuum conditions varying (1) the fraction of liquid Hg evaporated at 22 °C and (2) the temperature of evaporation (22–100 °C). Both, residual liquid and condensed vapor fractions were analyzed using stannous chloride CV-MC-ICP-MS.

Equilibrium evaporation showed a constant liquid–vapor fractionation factor ($\alpha_{202/198}$) of 1.00086 ± 0.00022 (2SD, $n = 6$) within the 0–22 °C range. The 22 °C dynamic evaporations experiments displayed Rayleigh distillation fractionation behavior with liquid–vapor $\alpha_{202/198} = 1.0067 \pm 0.0011$ (2SD), calculated from both residual and condensed vapor fractions. Our results confirm historical data (1920s) from Brönsted, Mulliken and coworkers on mercury isotopes separation using evaporation experiments, for which recalculated $\delta^{202}Hg'$ showed a liquid–vapor $\alpha_{202/198}$ of 1.0076 ± 0.0017 (2SD). This liquid–vapor $\alpha_{202/198}$ is significantly different from the expected kinetic $\alpha_{202/198}$ value ($(202/198)^{0.5} = 1.0101$). A conceptual evaporation model of back condensation fluxes within a thin layer at the liquid–vapor interface was used to explain this discrepancy. The $\delta^{202}Hg'$ of condensed vapor fractions in the 22–100 °C temperature range experiments showed a negative linear relationship with $10^6/T^2$, explained by increasing rates of exchange within the layer with the increase in temperature.

Evaporation experiments also resulted in non-mass-dependent fractionation (NMF) of odd ^{199}Hg and ^{201}Hg isotopes, expressed as $\Delta^{199}Hg'$ and $\Delta^{201}Hg'$, the deviation in ‰ from the mass fractionation relationship with even isotopes. Liquid–vapor equilibrium yielded $\Delta^{199}Hg'/\Delta^{201}Hg'$ relationship of 2.0 ± 0.6 (2SE), which is statistically not different from the one predicted for the nuclear field shift effect ($\Delta^{199}Hg/\Delta^{201}Hg \approx 2.47$). On the other hand, evaporation under dynamic conditions at 22 °C led to negative anomalies in the residual liquid fractions that are balanced by positive anomalies in condensed vapors with lower $\Delta^{199}Hg'/\Delta^{201}Hg'$ ratios of 1.2 ± 0.4 (2SD). This suggests that either magnetic isotope effects may have occurred without radical chemistry or an unknown NMF process on odd isotopes operated during liquid mercury evaporation.

1. INTRODUCTION

The geochemical cycling of mercury at the Earth's surface is dominated by atmospheric pathways and Hg^0 represents more than 60% of total anthropogenic gaseous mercury emitted (Lohman et al., 2008). Pacyna et al.

* Corresponding author. Address: Centre de Recherche Pétrographique et Géochimique, Nancy Université, CNRS UPR 2300, BP 20, 54501 Vandoeuvre les Nancy, France. Fax: +33 3 83 51 17 98.
E-mail address: nestrade@crpg.cnrs-nancy.fr (N. Estrade).

0016-7037/$ - see front matter © 2009 Elsevier Ltd. All rights reserved.
doi:10.1016/j.gca.2009.01.024

(2006) estimated that for the year 2000 global anthropogenic emissions were nearly 2200 T yr^{-1}, whereas Selin et al. (2007) estimated the global primary natural flux from land and sea to be 900 T yr^{-1}, although natural volcanic fluxes of 112–700 T yr^{-1} (Nriagu and Becker, 2003; Pyle and Mather, 2003) were not included in the latter. Anthropogenic emissions, mostly due to stationary combustion (notably coal), non-ferrous metal refining, cement production and gold mining, therefore represent approximately 58–71% of the total primary emissions. Evaporation (distillation) of liquid mercury can take place in a variety of industrial applications such as refining processes. Mercury has a high-saturated vapor pressure for a metal and is easily subject to liquid–vapor changes. The study of liquid mercury evaporation through a simple experimental setup should provide a first basis for isotopic fractionation in the liquid–vapor system.

Up to now, evaporation and condensation laboratory experiments have mainly been used to understand elemental and isotopic fractionation of extraterrestrial material in the context of solar nebula processes. High temperature evaporations have been conducted on Mg (Wang et al., 2001; Richter et al., 2002, 2007; Young et al., 2002) and on K isotopes (Yu et al., 2003), while moderate temperature evaporation (Wombacher et al., 2004) has been undertaken with cadmium metal. All of these studies showed substantial isotopic fractionation during evaporation and condensation, and in particular an enrichment of the lighter isotopes in the vapor phase.

Mercury evaporation experiments were already being conducted at the beginning of the 20th century in order to investigate the separation of isotopes. In 1920, the future Nobel Prize winner, J.N. Brönsted published with G. von Hevesy a short communication (Brönsted and von Hevesy, 1920), reporting that they had achieved the partial separation of Hg isotopes by vacuum evaporation of liquid mercury. A 14% Rayleigh evaporation yielded a light evaporated fraction with a density of 0.999980 times the original density, and a 75% evaporation yielded a residue that was heavier by a factor of 1.000031. These measurements were made by pycnometry, a highly precise method for determining relative density differences, with typical precision of ~1 ppm (density). Shortly afterwards, Brönsted and von Hevesy (1921), and Mulliken and Harkins (1922) published detailed articles on the theory and experiments of Hg evaporation and condensation. In these studies, the relative density of the lightest distillate and heaviest residue after multiple evaporation/condensation were reported to be −260 and +230 ppm, respectively. This amounts to approximately −84‰ and +74‰ on the $\delta^{202}Hg'$ scale.

The development of cold vapor multicollector ICP-MS (CV-MC-ICP-MS) has made possible high precision isotope abundance analysis of small amounts of Hg (Klaue et al., 2000). Since then, numerous studies have charted the large variation in natural mass-dependent fractionation (MDF) of Hg isotopes (~1.75‰/amu) and the processes that govern them (Lauretta et al., 2001; Hintelmann and Lu, 2003; Jackson et al., 2004; Smith et al., 2005; Xie et al., 2005; Foucher and Hintelmann, 2006; Kritee et al., 2007; Zheng et al., 2007; Smith et al., 2008; Sonke et al., 2008; Zambardi et al., 2008). Recent works denoted significant non-mass-dependent fractionation (NMF) of the odd isotopes (^{199}Hg and ^{201}Hg) of mercury in biogeological samples (Jackson et al., 2006; Bergquist and Blum, 2007; Epov et al., 2008; Biswas et al., 2008; Ghosh et al. 2008; Jackson et al., 2008). In contrast to MDF, which is governed by chemical energy of the starting and transition states of reactant molecules, NMF reported on Hg isotopes in experimental and natural processes have been suggested to result from either magnetic interactions (magnetic isotope effect) (Buchachenko et al., 2004; Bergquist and Blum, 2007; Buchachenko et al., 2007) or from nuclear volume effects (also known as nuclear field shift effect) (Schauble, 2007).

Here, isotopic fractionation of liquid elemental mercury during evaporation has been investigated under (1) atmospheric pressure at equilibrium and (2) under vacuum (10^{-5} bar) in a dynamic, non-equilibrium mode. Extent of fractionation, MDF and NMF are documented during equilibrium and kinetic evaporation of liquid mercury from 0 to 100 °C. We compare our results with historical data of Brönsted, Mulliken and coworkers and the current theories on MDF and NMF.

2. MATERIALS AND METHODS

2.1. Experimental evaporation

For the present study, a commercial liquid metal mercury solution (Rhône-Alpes Technologies) was used as the starting material for evaporation experiments. HNO_3 used was a 69% (weight) PROLABO® solution, NORMAPUR for trace analysis of Cd, Hg and Pb. All dilutions were undertaken with MilliQ water.

Two different types of evaporation were conducted. The first one, representing equilibrium evaporation (Fig. 1a), consisted of introducing 30 g of liquid mercury under atmospheric pressure into a 40 ml vessel, hermetically sealed by a Teflon lined septum. The temperature was held constant in the range 2–22 °C over 24 h in order to reach equilibrium ($P_{Hg} = P_{sat,Hg}$) between liquid mercury and its saturated vapor. Subsequently, the mercury vapor above the liquid was collected with a 10 ml Hamilton Gastight® syringe instantaneously injected and bubbled into a second hermetically sealed vessel which contained 1 ml concentrated HNO_3, then shaken for 10 h. An estimation of the amount of sampled gaseous Hg was done assuming saturation vapor pressure laws for liquid mercury ($\log(P) = 10.122–3190/T(K)$), Weast (1999). The collected vapor was adjusted to reach 10 μg L^{-1} after dilution. Final concentrations were measured with a Perkin-Elmer ELAN 6000 ICP-MS. Six samples in the 2–22 °C temperature range presented yields of dissolution more than 90 ± 10%. Due to the large volume of the syringe and the fact that several uptakes were necessary, a 10% concentration uncertainty is assumed. These yields allowed us to justify that equilibrium evaporation conditions were reached.

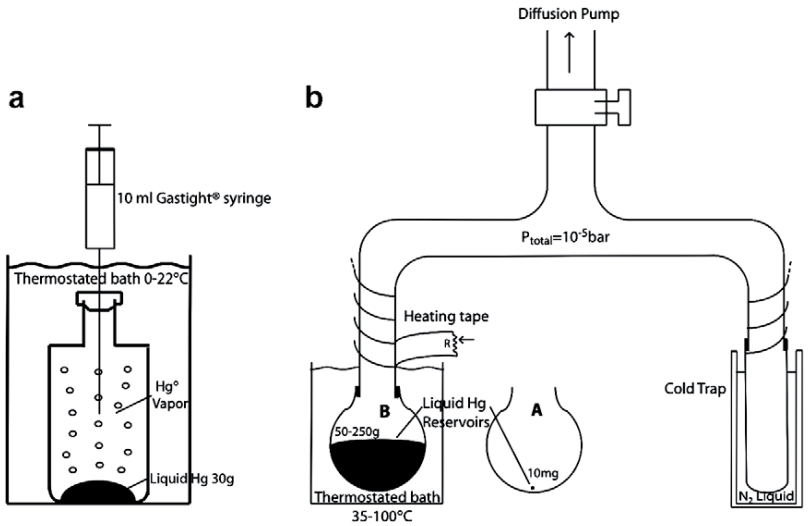

Fig. 1. A schematic of experimental evaporation systems. (a) *Equilibrium evaporation*: 30 g liquid Hg was introduced into a 40 ml glass vessel. Saturated vapor was taken up after 24 h equilibration at various temperatures (0–22 °C) and dissolved into nitric acid. (b) *Dynamic evaporation*: liquid Hg was evaporated under a vacuum of 10^{-5} bar and vapor was condensed onto the wall of a cold trap. Reactor A contained a ca. 10 mg liquid Hg droplet which evaporated at 22 °C between 6 and 24 h. Reactor B contained 250 g (or 50 g, see text) liquid Hg fractions which evaporated between 22 and 100 °C for a few minutes. A heating tape surrounded the glass tubing in order to maintain the temperature and prevent any Hg condensation outside the cold trap.

For the second type of evaporation, two dynamic experiments were performed in a closed system made of glass (Fig. 1b). Prior to each experiment, a weighted amount of liquid mercury reservoir was dipped into a −30 °C bath during 10 min and a 10^{-5} bar vacuum was reached in the system, using a diffusion pump. Then, the liquid mercury reservoir was isolated from the pump and held five minutes at the experimental temperature before the liquid nitrogen cold trap (−196 °C) was put into operation. Finally, the liquid mercury was continuously evaporated and its vapor condensed onto the wall of the cold trap (diameter 5 mm, length 10 cm). The condensed mercury vapor, which represents the cumulated evaporated fraction, was collected and dissolved in concentrated nitric acid. The evaporation glass line was cleaned in concentrated nitric acid bath after each run to prevent any contamination due to possible adsorption of mercury onto the tube wall.

The first set of experiments (Fig. 1b, reactor A) simulated a Rayleigh distillation. About 10 mg of liquid mercury (≈1 mm^3) was introduced into the reservoir and evaporated at 22 °C. Evaporation times were between 6 and 24 h and the fraction of mercury remaining in the liquid (f_{Hg}) was between 0.3 and 0.9. f_{Hg} was determined by two independent methods. The first one consisted of weighing with a precision scale (0.1 mg) the initial mercury reservoir and the residual liquid fraction. For the second one, residual liquid and evaporated fractions concentrations were precisely measured by MC-ICP-MS. Results with both methods were similar and the difference was considered as the error on the f_{Hg} determination. Both residual liquid and evaporated fractions were analyzed for their isotopic composition.

The second set of experiments (Fig. 1b, reactor B) investigated the temperature dependency of the liquid–vapor Hg isotope fractionation. Liquid mercury was introduced into the reservoir and dipped into a water bath heated at 100, 65, 50 and 35 °C. The connection tube between the Hg liquid reservoir and the cold trap was continuously heated with a heating tape at the experimental temperature to avoid any glass wall adsorption. Two different weights (250 and 50 g) of liquid mercury were evaporated at 22 °C. A 250 g sample was put into a large spherical volume reservoir with an evaporation surface of ca. 20 cm^2 and a 50 g sample was put into a small cylindrical sample volume reservoir with an evaporation surface of 3 cm^2. The evaporation times were approximately 5 min at 100 °C up to 1 h at 22 °C to recover a fraction of Hg remaining in the liquid around 0.999 in each experiment. For this second set of experiments, only condensed vapor fractions were analyzed.

2.2. Isotopic analysis

Isotopic measurements were conducted with a Thermo-Finnigan Neptune MC-ICP-MS at the Laboratoire de Mécanismes et Transfers en Géologie (LMTG) in Toulouse (France). A stannous chloride cold vapor generation system (Perkin-Elmer® FIAS-400MS) and a CETAC Aridus II desolvation unit were coupled directly to the MC-ICP-MS for mercury and thallium introduction, respectively. For most samples, isotopes 198, 199, 200, 201 and 202 for mercury and 203 and 205 for thallium were monitored with the static cup configuration (Table 1). Selected samples were analyzed for ^{204}Hg as well with a dynamic collection scheme (Table 1). Data acquisition utilized one block of 60 times 8 s integration cycles (8 min total). Bracketing reference and sample solutions were mono-elementary Hg

Table 1
Neptune cup configurations for static and for dynamic (targeted at ^{204}Hg) collection of Hg isotopes. Despite a dynamic range of 17 mass percent, the LMTG Neptune is constructed in the positioning of L4, L3, H3, H4, such that dynamic collection is necessary to measure ^{204}Hg.

	L4	L3	L2	L1	C	H1	H2	H3	H4
Static	—	^{198}Hg	^{199}Hg	^{200}Hg	^{201}Hg	^{202}Hg	^{203}Tl	^{205}Tl	—
Dynamic	—	^{200}Hg	^{201}Hg	^{202}Hg	^{203}Tl	^{204}Hg	^{205}Tl	^{207}Pb	—

(+II) solutions prepared in 5% nitric acid. Both reference and sample concentrations were adjusted to 10 μg L^{-1} for equilibrium experiments and to 25 μg L^{-1} for dynamic experiments. ^{202}Hg intensity was around 5 V at an uptake rate of 500 μL min^{-1}. Wash-out time after samples and reference solutions were 12 min, so that blank solution intensities were less than 1% of the reference and sample intensity. Instrumental mass bias on Hg isotopes was corrected using the exponential law, standard-sample bracketing, and continuous measurement of the $^{205/203}$Tl ratio from the isotopic certified standard reference material NIST 997. Variations in Hg isotopic composition are expressed relative to the standard reference material NIST SRM 3133, using the delta notation and following recent recommendations for Hg isotopes (Blum and Bergquist, 2007):

$$\delta^{X/198}(‰)_{sample/NIST3133} = \left(\frac{^{X/198}Hg_{sample}}{^{X/198}Hg_{NIST3133}} - 1\right) \times 1000 \quad (1)$$

where X represents Hg isotopes other than 198.

The external reproducibility of the method was determined using two fractionated isotopic in-house reference materials (RM). Measurements were done with concentrations between 5 and 25 ppb in 5–10% HNO_3 matrix during different sessions. Two standard deviation (2SD) on the δ^{202}Hg obtained with 10 measurements for these two RM were 0.22‰ (RM 1) and 0.26‰ (RM 2), 2SD on the δ^{199}Hg were, respectively, 0.03‰ and 0.04‰ and 2SD on the δ^{201}Hg were, respectively, 0.04‰ and 0.04‰ (see Section 3.3 non-mass-dependent fractionation for δ^{199}Hg and δ^{201}Hg definition). At the time of this study (2006), the secondary reference material UM-Almaden (Blum and Bergquist, 2007) was not available. More recent Hg isotope analysis on the LMTG Neptune showed excellent agreement with published values for UM-Almaden (Epov et al., 2008). External reproducibility of unknown samples reported is 2 standard error (2SE) of the mean value (calculated from different brackets of the sample), except when this value is below the external reproducibility of the method (Goldstein et al., 2003). In this case the 2SD values calculated for the RM 1 were used.

2.3. Evaporation laws

Evaporation and condensation are phase changes where mass transport processes (kinetic aspect) between and within phases take place, and during which isotopic fractionation can take place (Davis et al., 1990; Ozawa and Nagahara, 2001; Wang et al., 2001; Richter et al., 2002, 2007; Young et al., 2002; Richter, 2004; Wombacher et al., 2004). The kinetic theory of gases used here (as developed in Richter et al., 2002, 2007; Richter, 2004; Dauphas and Rouxel, 2006) aims to describe fluxes and rates of evaporation. The net evaporation flux of an element or an isotope i from a condensed phase to a surrounding gas is given by (Hertz–Knudsen equation):

$$J_i = n_i \gamma_i \frac{(P_{i,sat} - P_i)}{\sqrt{2\pi m_i RT}} \quad (2)$$

where J_i is the net evaporation flux of i in moles per unit area per unit time, n_i is the number of atoms of i in the gas species ($n_i = 1$, for all these gas species), γ_i is the evaporation coefficient of i, $P_{i,sat}$ is the saturated vapor pressures of i, P_i is the partial pressure of i at the evaporating surface, m_i the molar mass of gas species containing i, R is the gas constant and T is absolute temperature. Different critical evaporation regimes can be considered. One limiting case is reached in the vacuum limit, $P_i << P_{i,sat}$, which represents free evaporation. Then, the ratio of the evaporation flux of two isotopes indicated by the subscripts 1 and 2, is

$$\frac{J_1}{J_2} = \frac{\gamma_1}{\gamma_2}\left(\frac{P_{1,sat}}{P_{2,sat}}\right)\sqrt{\frac{m_2}{m_1}} \quad (3)$$

where J_1 and J_2 are the evaporation flux, γ_1 and γ_2 are the evaporation coefficients, $P_{1,sat}$ and $P_{2,sat}$ the saturated vapor pressures and m_1 and m_2 the molar masses of the two isotopes. Equilibrium evaporation represents the case where partial pressure tends towards saturated vapor pressure ($P_1 \rightarrow P_{1,sat}$), thus the net evaporation flux tends towards zero. The fractionation factor between a condensed phase and the surrounding gas in the vacuum limit is defined as the ratio of the flux of the two isotopes, J_1/J_2, divided by the atom ratio of the isotopes in the condensed phase. Under equilibrium conditions, the isotopic fractionation factor represents the ratio of the atom ratio in the gas phase and in the liquid phase. In a closed system, the expression of the atom ratio in the gas phase is equivalent to the ratio of saturated vapor pressure of each isotope. The equilibrium isotopic fractionation factor is defined by:

$$\alpha^{Eq}_{1/2} = \left(\frac{N_1}{N_2}\right)_{vap} \Big/ \left(\frac{N_1}{N_2}\right)_{liq} = \left(\frac{P_{1,sat}}{P_{2,sat}}\right) \Big/ \left(\frac{N_1}{N_2}\right)_{liq} \quad (4)$$

where $(N_1/N_2)_{liq}$ is the isotopic ratio in the condensed phase. Note that as $P_{1,sat}$ and $P_{2,sat}$ are only function of temperature, $P_{1,sat}/P_{2,sat}$ is the isotopic ratio of the gas phase. Using Eqs. (3) and (4), the kinetic isotope fractionation factor of the evaporated fraction relative to the liquid source is then defined as

$$\alpha_{1/2} = \left(\frac{J_1}{J_2}\right) \Big/ \left(\frac{N_1}{N_2}\right) = \alpha^{Eq}_{1/2}\left(\frac{\gamma_1}{\gamma_2}\right)\sqrt{\frac{m_2}{m_1}} = \alpha^{Eq}_{1/2}\alpha^{Kin}_{1/2} \quad (5)$$

To a first approximation, evaporation coefficients are usually assumed to be equal for the isotopes of a same element and in our case the fractionation factors (equilibrium, kinetic and total) are now defined relative to the gas phase as:

$$\alpha_{1/2}^{\mathrm{Eq}} = \left(\frac{N_1}{N_2}\right) \Big/ \left(\frac{P_{1,\mathrm{sat}}}{P_{2,\mathrm{sat}}}\right), \quad \alpha_{1/2}^{\mathrm{Kin}} = \sqrt{\frac{m_1}{m_2}} \quad \text{and} \quad \alpha_{1/2}^{\mathrm{total}} = \frac{R_{12,\mathrm{liq}}}{R_{12,\mathrm{vap}}} = \alpha_{1/2}^{\mathrm{Eq}} \sqrt{\frac{m_1}{m_2}} \tag{6}$$

In order to determine fractionation factors, Rayleigh distillation equations were used to simulate the evolution of isotope ratios data from this study and of the historical data. Equations for Rayleigh type distillations apply to the remaining liquid phase (Eq. (7)), the instantaneous vapor (Eq. (8)) and the cumulative vapor that is condensed into the cold trap (Eq. (9)) (Hoefs et al., 1987):

$$R_l = R_{l_0} \times f^{(\frac{1}{\alpha}-1)} \tag{7}$$

$$R_v = R_{l_0} \times \frac{1}{\alpha} \times f^{(\frac{1}{\alpha}-1)} \tag{8}$$

$$\overline{R_v} = R_{l_0} \times \frac{1-f^{\frac{1}{\alpha}}}{1-f} \tag{9}$$

where f is the fraction of Hg remaining in the liquid, α is the fractionation factor between liquid and vapor, R_{l_0} is isotopic ratio of the starting liquid, R_l is the instantaneous isotopic ratio in the liquid, R_v is the instantaneous isotopic ratio in the vapor and R_v is the cumulated isotopic ratio in the vapor. These relations are easily converted into delta notation, $\delta = (R/R_{l_0} - 1)10^3$.

2.4. Isotope fractionation laws

Isotope fractionation laws have been the subject of numerous studies, particularly for describing mass-dependent kinetic and equilibrium fractionations (e.g., Urey, 1947; Bigeleisen, 1949; Young et al., 2002; Schauble, 2004). Furthermore, non-mass-dependent isotopic fractionation (NMF) for Hg isotopes by (i) the nuclear volume (NV) fractionation mechanism has been investigated by Bigeleisen (1996) and Schauble (2007) and (ii) the magnetic isotope effect by Buchachenko et al. (1976), Turro and Kraeutler (1978), Turro (1993), Buchachenko (1995), Buchachenko (2001). Isotope fractionation mechanisms are summarized in the following and precisions are given on NMF processes.

Generally, fractionation between two isotopic ratios with a common isotope denominator is described by a power law (Young et al., 2002):

$$\alpha_{2/1} = (\alpha_{3/1})^{\beta} \tag{10}$$

where α is the fractionation factor of the isotopic ratio of two species or two reservoirs. The exponent β varies with the fractionation process and represents the slope of a fractionation line in a linearized three-isotope diagram. In this study, the range of delta values measured (δ^{202}Hg) exceed 5‰, thus linearized delta values, denoted as 'delta prime' (δ'), have been used based on the formula given by Young and Galy (2004): $\delta' = 10^3 \ln((\delta + 10^3)/\ 10^3)$.

In the case of an ideal gas without interaction, the mass-dependent physical kinetic (mass transport process) isotope fractionation, β (Table 2) is defined as:

$$\beta_{\mathrm{Kin}} = \frac{\ln\left(\frac{m_1}{m_2}\right)}{\ln\left(\frac{m_1}{m_3}\right)} \tag{11}$$

in the case of mass-dependent equilibrium fractionation, β (Table 2) is defined as:

$$\beta_{\mathrm{Eq,MD}} = \frac{\left(\frac{1}{m_1} - \frac{1}{m_2}\right)}{\left(\frac{1}{m_1} - \frac{1}{m_3}\right)} \tag{12}$$

As suggested by Schauble (2007), the natural isotopic variations of very heavy elements such as Hg ($Z = 80$) and Tl ($Z = 81$) of up to 1.75‰/amu are difficult to reconcile by equilibrium MDF. In a recent revision of the theory of first-order mass-dependent fractionation, Bigeleisen (1996) evaluated another isotope fractionation mechanism, named the nuclear volume effect (NV, or nuclear field shift effect), to explain the isotopic shifts reported in the electronic spectra of heavy elements. This type of fractionation results in a displacement of the ground electronic energy of an atom or molecule due to the nuclear sizes and shapes of isotopes. The nuclear charge radii, and thus nuclear volumes, of the even isotopes ^{198}Hg, ^{200}Hg and ^{202}Hg increase almost perfectly linearly with isotope mass (Angeli, 2004). The odd isotopes ^{199}Hg and ^{201}Hg however, have a smaller nuclear volume than expected from this linear relationship. Consequently, the relative nuclear charge density is larger for the ^{199}Hg and ^{201}Hg isotopes and results in a stronger pull on the valence band electrons that participate in chemical bonding. With their valence electrons spending relatively more time in the nucleus, the ^{199}Hg and ^{201}Hg isotopes tend to form weaker bonds than the ^{198}Hg, ^{200}Hg and ^{200}Hg isotopes. Schauble (2007) calculated MDF and nuclear volume NMF for solvated, halogenated or methyl mercury species relative to mercury vapor at equilibrium and emphasized the dominant role of the nuclear volume fractionation for the super heavy elements. In terms of the isotope fractionation law (Eq. (10)), Schauble (2007) defined β values for Eq. (10) (Table 2) depending upon nuclear charge radii as:

$$\beta_{\mathrm{NV}} = \frac{\langle r_1^2 \rangle - \langle r_2^2 \rangle}{\langle r_1^2 \rangle - \langle r_3^2 \rangle} \tag{13}$$

where $\langle r^2 \rangle$ is the mean square charge radii (fm^2) of the isotopes. However, based on a compilation of nuclear charge radii by Angeli (2004), Schauble (2007) suggested that nuclear volume fractionation will differ from mass dependency for ^{196}Hg, ^{199}Hg, ^{201}Hg and ^{204}Hg when normalized to ^{198}Hg. Whereas ^{196}Hg is typically not measured due to its low abundance, ^{204}Hg data has been reported and shown to display MDF rather than NMF anomalies, even in the presence of large ^{199}Hg, and ^{201}Hg NMF anomalies (Bergquist and Blum, 2007; Ghosh et al., 2008). Ghosh et al. (2008), pointed recently out that Angeli's (2004) statistically

Table 2
β Factors values for equilibrium and kinetic mass-dependent fractionation, nuclear volume fractionation and magnetic isotope effect processes relative to $^{202/198}$Hg.

	$^{196/198}$Hg	$^{199/198}$Hg	$^{200/198}$Hg	$^{201/198}$Hg	$^{202/198}$Hg	$^{204/198}$Hg
Mass-dependent equilibrium	−0.5151	0.2539	0.50493	0.7539	1.0000	1.4855
Mass-dependent kinetic	−0.5074	0.2520	0.5024	0.7520	1.0000	1.4928
Nuclear volume (Angeli, 2004)	−0.4660	0.1076	0.4966	0.7003	1.0000	1.6543
Nuclear volume (Hahnet al., 1979)	n.d.	0.0804	0.4712	0.6838	1.0000	1.4994
Magnetic isotope effect	?	?	?	?	?	?

determined nuclear charge radii agree with experimentally determined radii (Hahn et al., 1979), except for ^{204}Hg. They suggested that no ^{204}Hg NMF anomaly is to be expected during NV fractionation. The improved NV scaling factors by Ghosh et al. (2008) apply to isotope fractionation factors with ^{202}Hg as the reference isotope. Here (Table 2) we re-evaluated NV scaling factors (β_{NV}, Eq. (13)) for the recently recommended Hg stable isotope reporting guidelines, using ^{198}Hg as the reference isotope in the denominator (Blum and Bergquist, 2007). Note the absence of deviations from MDF in β_{NV} for ^{204}Hg, using Hahn's (1979) data. The sensitivity of predicted nuclear volume Hg isotope anomalies to the nuclear charge radii, suggests that caution should be taken in identifying NV effects in natural or experimental Hg NMF observations.

Another type of NMF has been discovered in the mid-1970's and is called magnetic isotope effect (MIE) because it separates isotopes into different reaction products according to their spin and magnetic moment. MIE is based on the spin conservation principle between reactants and products in a reaction involving Hg radicals. During radical reactions, stable reactants absorb energy (thermal, photons) to produce a radical pair of reactants (R··R) in the triplet state. Although back transformation into the original reactants is technically spin-forbidden, strong spin–orbit coupling in Hg can induce triplet singlet conversion and back reaction for all Hg isotopes. Nuclei with odd neutron numbers exhibit nonzero nuclear spin quantum numbers 'I' and have nuclear magnetic moments, μ, that interact with electron magnetic moments through the nuclear-electron hyperfine coupling. Mercury has two odd neutron number isotopes (^{199}Hg and ^{201}Hg), which have nuclear spins 1/2 and 3/2 and magnetic moments of +0.5029 and −0.5602 μ_B, respectively, and subject to the magnetic isotope effect. Triplet-singlet conversion of magnetic radical pairs (^{odd}Hg) is enhanced and magnetic. Magnetic pairs are therefore also more probable to recombine into the starting molecules, while nonmagnetic pairs are more likely to form reaction products via dissociation of R··R into free radicals. Due to the difference in the rates of spin conversion, isotopes with magnetic and nonmagnetic are separated and accumulation of magnetic versus nonmagnetic isotopes can be generated in products and reactants (Buchachenko, 1995; Buchachenko, 2000; Buchachenko, 2001).

The magnetic isotope effect for mercury has been investigated and claimed to be observed in the reaction of kreatine kinase and methylmercury by gas source mass spectrometry (Buchachenko et al., 2004) and in the photolysis of Bis(*p*-trifluoromethylbenzyl)mercury by nuclear magnetic resonance (Buchachenko et al., 2007). Hg isotope fractionation during photoreduction of Hg^{2+} and MeHg in the presence of dissolved organic carbon (DOC) in aqueous solution was conducted by Bergquist and Blum (2007) using CV-MC-ICP-MS and showed ^{199}Hg and ^{201}Hg isotope enrichment for mercury remaining in solution relative to MDF. The authors suggested MIE as the underlying NMF mechanism, based on the analogy between aquatic Hg photoreduction and the understanding of MIE during radical chemistry.

2.5. Extracting data from historical experiments

The isotope separation theories developed by Brönsted, Harkins and coworkers in their remarkable papers used a nomenclature aimed at describing relative density differences (kg m^{-3}), based on separation coefficients. The original density data are summarized in Appendix A Table 1. We assume that their liquid Hg source had an IUPAC isotopic composition, and associated isotope ratios R. Initially we chose physical kinetic isotope fractionation as the governing mass fractionation law (Eq. (11)). The evolving isotopic composition of IUPAC Hg during Rayleigh distillation can be simulated in terms of isotope ratios R as described above (Eqs. (7)–(9)). Once this has been achieved we calculated the densities that correspond to the isotopically fractionated Hg residues and condensed vapors as follows: first, isotopic abundances, Ab_x, are calculated from the isotope ratios for each fractionated sample. Density contributions, $\rho_{c,x}$ (g cm^{-3}), for each isotope 'x' can then be calculated:

$$\rho_{c,x} = \frac{m_x Ab_x}{V_{Hg}} \tag{14}$$

where V_{Hg} is the constant atomic volume for Hg isotopes of 14.8222 cm^3 mol^{-1}, and m_x are the isotope masses (g mol^{-1}). The atomic volume (not to be confused with nuclear volume) was calculated by dividing the atomic weight of IUPAC Hg (200.5927 g mol^{-1}) by an assumed density of this starting material (13.5400 g cm^{-3} at 25 °C, CRC Handbook of Physics and Chemistry). Finally summing all density contributions yields the density (kg m^{-3}) for a fractionated Hg sample:

$$\rho_{sim,Hg} = \sum_x \rho_x \tag{15}$$

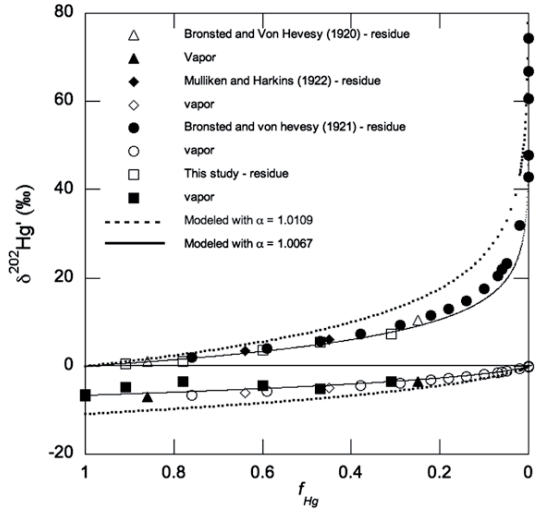

Fig. A1. Selected historical and new data for liquid Hg evaporation from Table A1 reported in a Rayleigh diagram. Original density data are recalculated on the $\delta^{202}Hg'$ scale. The black line denotes the isotopic evolution of residual liquid and vapor Hg using a fractionation factor of 1.0067, as experimentally measured in this study, whereas the gray dashed line marks the isotopic evolution of residual liquid and vapor Hg using a fractionation factor of 1.0109, as theoretically expected for pure kinetic fractionation.

The simulated densities, $\rho_{sim,Hg}$ of fractionated Hg can be directly compared to the measured experimental densities, $\rho_{exp,Hg}$ by Brönsted and von Hevesy (1920), Brönsted and von Hevesy (1921), and by Mulliken and Harkins (1922). Initially all historical data points were fitted together, by optimizing one adjustable parameter, $\alpha_{liq-vap}$ until the root mean square error (RMSE) between $\rho_{exp,Hg}$ and $\rho_{sim,Hg}$ reached a minimum value. The resulting fitted $\alpha_{liq-vap}$ for physical kinetic mass-dependent Hg isotope fractionation is 1.0076 ± 0.0017 (2SD, $n = 6$). Sensitivity testing shows that the assumed IUPAC isotopic abundances and density of the historical starting material does not influence the outcome of $\alpha_{liq-vap}$, because all analytical measurements involve relative changes in density. Fig. A1 illustrates recalculated data for the historical dataset on the $\delta^{202}Hg'$ scale (see also Table 1). The heaviest residue measured is $+74‰$ on the $\delta^{202}Hg'$ scale (Fig. A1), while the lightest vapor obtained after sequential distillations reached $-84‰$ (not shown).

3. RESULTS

In the following sections, the Hg isotopic composition of residual Hg^0(liq) fractions and condensed Hg^0(vap) fractions are reported relative to the isotopic composition of the initial liquid mercury. Scale translation was determined using:

$$\delta^{202}Hg'_{sample/Initial\ Hg} = \delta^{202}Hg'_{sample/NIST\ 3133} - \delta^{202}Hg'_{Initial\ Hg/NIST\ 3133} \quad (16)$$

This approximation is valid because $\delta^{202}Hg'_{initial\ Hg/NIST\ 3133}$ is small ($-1.06 \pm 0.22‰$ (2SD), Table 2). Furthermore, the starting material does not present NMF ($\Delta^{199}Hg' = 0.01 \pm 0.03‰$, $\Delta^{201}Hg' = -0.01 \pm 0.04‰$).

3.1. Equilibrium evaporation experiments

Six samples of Hg^0(vap) above the liquid mercury sampled at equilibrium between 2 and 22 °C have been analyzed. Linearized delta values of the saturated vapor relative to the starting liquid between 2 and 22 °C are listed in Table 3 and presented in Fig. A2 against temperature. For all experiments, the saturated Hg^0(vap) is enriched in the light isotopes relative to liquid mercury. Furthermore, all results are identical within analytical errors. The average $\delta^{202}Hg'$ of saturated vapor relative to the liquid is $-0.86 \pm 0.22‰$ (2SD, $n = 6$). Thus, the average liquid–va-

Table 3
Isotopic compositions of the starting liquid Hg relative to the NIST 3133, and isotopic composition of the vapor above liquid Hg under equilibrium conditions between 2 and 22 °C relative to the starting liquid.

Sample	T (°C)	n[b]	$\delta^{199}Hg'$	2SE	$\delta^{200}Hg'$	2SE	$\delta^{201}Hg'$	2SE	$\delta^{202}Hg'$	2SE	$\Delta^{199}Hg'$[e]	2SE	$\Delta^{200}Hg'$[e]	2SE	$\Delta^{201}Hg'$[e]	2SE
Starting material[c] equilibrium[d]	20	3	−0.26	0.06*	−0.52	0.11*	−0.82	0.18*	−1.06	0.22*	0.01	0.03*	0.02	0.06*	−0.01	0.04*
1[a]	2.0	1	−0.10	0.06	−0.41	0.11	−0.58	0.18	−0.87	0.22	0.12	0.03	0.03	0.06	0.08	0.04
2[a]	7.2	1	−0.09	0.06	−0.40	0.11	−0.56	0.18	−0.83	0.22	0.12	0.03	0.02	0.06	0.07	0.04
3[a]	7.5	1	−0.10	0.06	−0.46	0.11	−0.62	0.18	−0.90	0.22	0.12	0.03	0.00	0.06	0.06	0.04
4[a]	11.4	1	−0.10	0.06	−0.43	0.11	−0.57	0.18	−0.87	0.22	0.12	0.03	0.01	0.06	0.08	0.04
5[a]	22.0	1	−0.12	0.06	−0.46	0.11	−0.59	0.18	−0.87	0.22	0.10	0.03	−0.02	0.06	0.07	0.04
6[a]	22.0	1	−0.07	0.06	−0.41	0.11	−0.58	0.18	−0.83	0.22	0.14	0.03	0.01	0.06	0.04	0.04
Average[f]	2–22		**−0.10**	0.06	**−0.43**	0.11	**−0.59**	0.18	**−0.86**	0.22	**0.12**	0.03	**0.01**	0.06	**0.07**	0.04

[a] 2SD RM 1 value (see Part 2.2).
[b] Number of measurements.
[c] Isotopic composition relative to NIST 3133.
[d] Isotopic composition relative to starting material.
[e] $\Delta^{199,200,201}Hg'$ are calculated relative to equilibrium MDF process.
[f] 2SE on the average of the six measurements is below the 2SD RM 1 value, 2SD RM 1 value is reported.

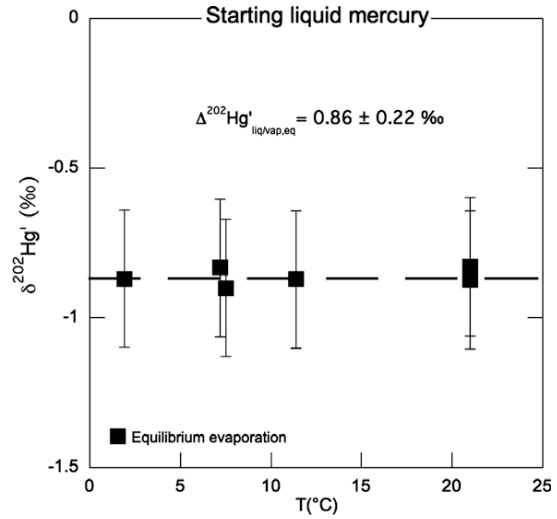

Fig. A2. The Hg isotopic composition ($\delta^{202}Hg'$) of the saturated vapor relative to the starting liquid as a function of temperature. Error bars correspond to the 2SD reported on RM1 (Table 2). Saturated vapor is enriched in light isotopes relative to the liquid and $\delta^{202}Hg'$ do not present a systematic variation with temperature (within error) in the range 2–22°C. The equilibrium liquid–vapor fractionation factor is 1.000 86 ± 0.000 22 (2SD).

por fractionation factor at equilibrium is $\alpha^{Eq}_{liq-vap} = 1.000\ 86 \pm 0.000\ 22$ for the $^{202/198}Hg$ isotope pair from 2 to 22 °C.

3.2. Dynamic evaporation experiments

Dynamic experiments were performed under a vacuum of 10^{-5} bar by continuous cryogenic pumping of the liquid mercury stock. The first set of experiments was undertaken at 22 °C and various fractions of residual liquid mercury (f_{Hg}) were obtained. Evaporation flux, linearized delta values of the remaining liquid and condensed vapor relative to the starting liquid are listed in Table 4.

Evaporation fluxes have been calculated using the approximation that the evaporating surface was a half sphere of 1 mm radius. Overall, experiments conducted at 22 °C present evaporation fluxes within the range 2–8×10^{-6} mol cm^{-2} s^{-1}. Residual liquid fractions show a range of isotopic fractionation ($\delta^{202}Hg'$) from 0‰ at $f_{Hg} = 1$ (starting liquid) to +7.23 ± 0.22‰ at $f_{Hg} = 0.3$. According to Eq. (7), isotopic compositions of residual liquid fractions $\ln R$ are plotted versus $-\ln f_{Hg}$ in Fig. 2, where R represents $(1 + \delta^{202}Hg'/1000)$. This diagram shows a linear relationship, which points out that liquid–vapor evaporation under a 10^{-5} bar vacuum, complies with Rayleigh fractionation behavior. A constant fractionation factor between phases was extracted from the slope $(1 - 1/\alpha)$ using Isoplot® X-Y regression software. The uncertainties of f_{Hg} and $\delta^{202}Hg'$ were taken into account by the software. The liquid–vapor fractionation factor under dynamic conditions is $\alpha_{liq/vap} = 1.0067 \pm 0.0011$ (2SD) for $^{202/198}Hg$. Therefore, at 22 °C and under dynamic conditions, the vapor is enriched in the lighter Hg isotopes by -6.7 ± 1.1‰ for $\delta^{202}Hg'$. This liquid–vapor fractionation factor is signif-

Table 4
Isotopic compositions of instantaneous residual liquid fractions and cumulated condensed vapor fractions under dynamic conditions at 22°C relative to the starting liquid Hg.

Sample	Evaporation time (h)	F	J^a (mol cm^{-2} s^{-1})	n^b	$\delta^{199}Hg'$	2SE	$\delta^{200}Hg'$	2SE	$\delta^{201}Hg'$	2SE	$\delta^{202}Hg'$	2SE	$\Delta^{199}Hg'^c$	2SE	$\Delta^{200}Hg'^c$	2SE	$\Delta^{201}Hg'^c$	2SE
Instantaneous residual liquid fractions																		
A	24	0.31 ± 0.03	3.5×10^{-6}	2	1.71	0.06*	3.60	0.11*	5.34	0.18*	7.23	0.22*	−0.12	0.03*	−0.03	0.06*	−0.09	0.04*
B	14	0.47 ± 0.05	8.3×10^{-6}	2	1.29	0.11	2.72	0.17	4.02	0.28	5.45	0.33	−0.09	0.03*	−0.02	0.06*	−0.08	0.04*
C	24	0.60 ± 0.02	7.1×10^{-6}	10	0.87	0.11	1.87	0.15	2.75	0.19	3.71	0.27	−0.07	0.03*	0.00	0.06*	−0.05	0.04*
D	17	0.78 ± 0.02	1.4×10^{-6}	2	0.24	0.06*	0.56	0.11*	0.87	0.18*	1.14	0.22*	−0.04	0.03*	−0.01	0.06*	0.01	0.04*
E	6	0.91 ± 0.02	2.1×10^{-6}	1	0.12	0.06*	0.28	0.11*	0.41	0.18*	0.56	0.22*	−0.02	0.03*	−0.01	0.06*	−0.01	0.04*
Cumulated condensed vapor fractions																		
A′	24	0.31 ± 0.03		2	−0.85	0.06*	−1.78	0.11*	−2.64	0.18*	−3.56	0.22*	0.05	0.03*	0.01	0.06*	0.03	0.04*
B′	14	0.47 ± 0.05		1	−1.22	0.06*	−2.56	0.11*	−3.79	0.18*	−5.11	0.22*	0.07	0.03*	0.00	0.06*	0.05	0.04*
C′	24	0.60 ± 0.02		2	−1.04	0.06*	−2.18	0.11*	−3.21	0.18*	−4.34	0.22*	0.05	0.03*	0.00	0.06*	0.06	0.04*
D′	17	0.78 ± 0.02		2	−0.81	0.06*	−1.73	0.11*	−2.56	0.18*	−3.44	0.22*	0.05	0.03*	0.00	0.06*	0.03	0.04*
E′	6	0.91 ± 0.02		2	−1.14	0.06*	−2.40	0.11*	−3.53	0.18*	−4.76	0.22*	0.06	0.03*	0.00	0.06*	0.05	0.04*

* 2SE on the average of the n measurements is below the 2SD RM 1 value, 2SD RM 1 value is reported (see Part 2.2).
[a] Net evaporation flux are calculated using approximation that evaporation surface was a half sphere of 1 mm radius and have to take into account as an estimation.
[b] Number of measurements.
[c] $\Delta^{199,200,201}Hg'$ are calculated relative to kinetic MDF process.

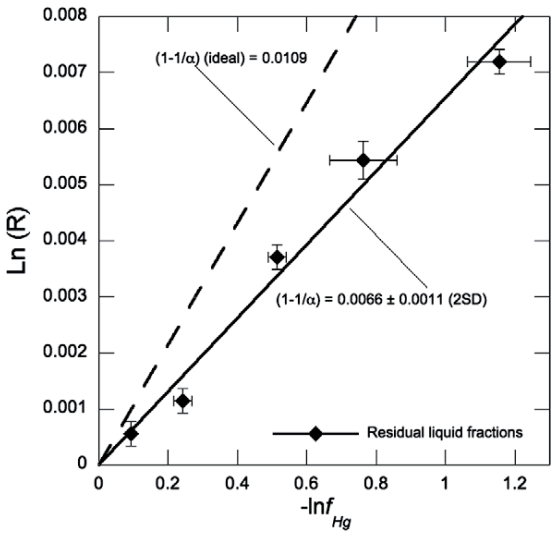

Fig. 2. The Hg isotopic composition of residual liquid fractions evaporated at 22 °C (Table 3) plotted as $\ln R$ against $-\ln f_{Hg}$, where f_{Hg} represent the fraction of Hg remaining in the liquid and R represents $(1 + \delta^{202}Hg'/1000)$. According to Eq. (7), a linear relationship indicates that the evolution of isotopic fractionation follows a Rayleigh distillation behavior with a constant fractionation factor, represented by the slope $(1 - 1/\alpha)$ and calculated using the X–Y Isoplot regression software. The obtained liquid–vapor $\alpha_{202/198}$ of 1.0067 ± 0.0011 (2SD) (black line) is significantly different from the global fractionation factor value ($\alpha_{202/198,\ global} = \alpha_{Eq}\ (202/198)^{0.5} = 1.0109$) (black dashed line) expected in an open system.

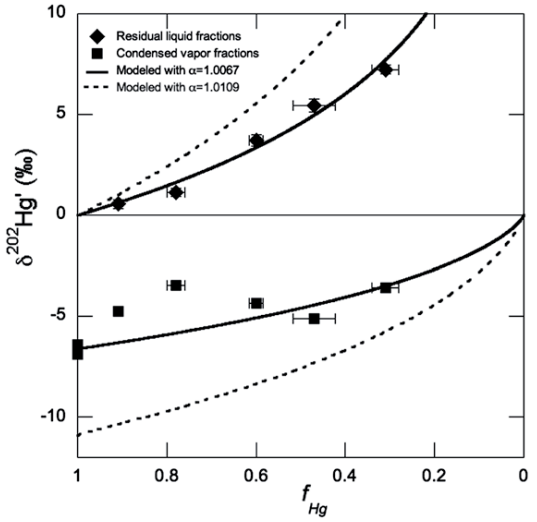

Fig. 3. A common Rayleigh isotope diagram where residual liquid and condensed vapor fractions isotope compositions ($\delta^{202}Hg$') are plotted as a function of the fraction of Hg remaining in the liquid (f_{Hg}) (evaporated at 22°C). Two $f_{Hg} = 1$ condensed vapor fractions display $\delta^{202}Hg' = -6.6 \pm 0.7‰$ (2SD), which fit with modeled evolution of isotopic compositions using Eq. (7) and liquid–vapor $\alpha_{202/198} = 1.0067$ (black line). This confirms the discrepancy with expected $\alpha_{202/198}$, value (1.0109) (gray dashed line).

icantly different from equilibrium evaporation where vapor was enriched only by 0.86‰ in the lighter isotopes. In addition, the value of 1.0067 is statistically not different from the fitted value of 1.0076 ± 0.0017 (2SD) for the historical data (see also Fig. A1).

Fig. 3 illustrates a common Rayleigh diagram where isotopic compositions ($\delta^{202}Hg'$) of residual liquid and evaporated fractions are plotted versus f_{Hg}. In this diagram, isotopic compositions evolution of residual liquid and evaporated fractions are modeled using Eqs. (7) and (9), respectively, with $\alpha = 1.0067$. Two evaporated fractions at 22 °C and $f = 1$ (see Table 5) show an average isotopic composition of $-6.6 \pm 0.7‰$ (2SD) ($\delta^{202}Hg'$). This value represents the isotopic fractionation between the liquid and the vapor and defines a fractionation factor of 1.0066 ± 0.0007 (2SD), which is in good agreement with the value of 1.0067 ± 0.0011 (2SD), determined independently from residual liquid fractions.

A theoretical overall fractionation factor under dynamic conditions can be calculated, using Eq. (6) and the equilibrium fractionation factor of 1.00086 previously determined. This yields a value of $\alpha_{theory} = 1.0109$, which is significantly larger than the two experimental fractionation factors measured in this study (1.0067 ± 0.0011 and 1.0066 ± 0.0007) and the historical experiments (1.0076 ± 0.0017, (2SD)). Figs. 2 and 3 show this discrepancy with modeled isotopic evolution calculated with $\alpha_{theory} = 1.0109$. Similar disagreement between theoretical and experimental α has been observed during evaporation of Mg (e.g. Davis et al., 1990; Wang et al., 2001; Richter et al., 2002; Richter et al., 2007) and Cd (Wombacher et al., 2008).

Fig. 3 illustrates also that the isotopic compositions of vapor condensed fractions ($f_{Hg} = 0.91$ and $f_{Hg} = 0.78$) poorly fit with the modeled Rayleigh curve ($\alpha_{liq/vap} = .0067 \pm 0.0011$), while vapor condensed fractions with $f_{Hg} < 0.78$ are not significantly different from the Rayleigh curve. These two fractions present a heavy isotope enrichment relative to the expected isotopic compositions. Moreover, the complementary residual liquid fractions for $f_{Hg} = 0.91$ and $f_{Hg} = 0.78$ do not show light isotope enrichment. These results suggest that condensation of Hg vapor in the cold trap may not have been quantitative and that the vapor Hg isotopic composition was slightly affected during its way to the cold trap.

The second set of dynamic experiments was done at the 22–100 °C temperature range with a 250 g liquid mercury reservoir at $f_{Hg} \approx 1$, such that the isotopic composition of the liquid mercury reservoir was not measurably modified between each run. Evaporation flux and delta values are listed in Table 5. Delta values for each temperature replicate were homogeneous within analytical error. Here, evaporation fluxes have been calculated using the approximation that the evaporating surface was a disk of 20 cm^2. The evaporation of larger amount of liquid Hg at 22 °C resulted in a 10 times lower Hg flux (mean of 0.35×10^{-6} mol cm^{-2} s^{-1}) than the small evaporating surface experiments, also conducted at 22 °C (mean of 4.5×10^{-6} mol cm^{-2} s^{-1}). The 100 °C experiment induced evaporation fluxes of 2×10^{-6} mol cm^{-2} s^{-1} similar to the small surface evaporation.

Table 5
Isotopic compositions of cumulated condensed vapor fractions under dynamic conditions between 22 and 100 °C relative to the starting liquid Hg.

Sample	T (°C)	Evaporation time (min)	J[a] (mol cm^{-2} s^{-1})	n[b]	δ^{199}Hg′	2SE	δ^{200}Hg′	2SE	δ^{201}Hg′	2SE	δ^{202}Hg′	2SE	Δ^{199}Hg′[c]	2SE	Δ^{200}Hg′[c]	2SE	Δ^{201}Hg′[c]	2SE
T100[e]	100	2	2.1×10^{-6}	2	−0.13	0.06*	−0.39	0.11*	−0.58	0.18*	−0.79	0.22*	0.07	0.03*	0.01	0.06*	0.02	0.04*
T65-1	65	15	2.2×10^{-6}	2	−0.52	0.06*	−1.19	0.11*	−1.73	0.18*	−2.37	0.22*	0.07	0.03*	0.01	0.06*	0.05	0.04*
T65-2	65	15	2.5×10^{-6}	10	−0. 56	0.06*	−1.25	0.11*	−1.84	0.18*	−2.51	0.22*	0.08	0.03*	0.01	0.06*	0.05	0.04*
T65	65				−0.54	0.06*	−1.22	0.11*	−1.79	0.18*	−2.44	0.22*	0.08	0.03*	0.02	0.06*	0.04	0.04*
T50-1	50	30	1.4×10^{-6}	3	−1.04	0.09	−2.13	0.17	−3.16	0.24	−4.25	0.34	0.03	0.06	0.01	0.02	0.03	0.07
T50-2	50	10	0.2×10^{-6}	3	−0.98	0.15	−2.02	0.25	−2.97	0.42	−3.98	0.51	0.03	0.03	0.00	0.02	0.03	0.05
T50-3	50	10	0.3×10^{-6}	3	−1.04	0.10	−2.18	0.19	−3.22	0.27	−4.34	0.38	0.05	0.05	0.01	0.01	0.04	0.06
T50	50				−1.02	0.07	−2.11	0.17	−3.12	0.27	−4.19	0.37	0.04	0.02	0.01	0.02	0.03	0.01
T35-1	35	15	0.3×10^{-6}	3	−1.35	0.07	−2.77	0.18	−4.11	0.29	−5.51	0.39	0.03	0.08	0.01	0.02	0.03	0.04
T35-2	35	15	0.3×10^{-6}	2	−1.31	0.13	−2.69	0.05	−4.01	0.18	−5.34	0.22	0.03	0.03	0.00	0.06	0.01	0.04
T35	35				−1.33	0.06	−2.73	0.11	−4.05	0.15	−5.41	0.24	0.03	0.00	0.01	0.01	0.02	0.03
T22-A[d]	22	57	0.5×10^{-6}	3	−1.54	0.06*	−3.20	0.11*	−4.77	0.18*	−6.40	0.22*	0.08	0.03*	0.02	0.06*	0.04	0.04*
T22-B[d]	22	60	0.2×10^{-6}	2	−1.67	0.06*	−3.46	0.11*	−5.13	0.18*	−6.89	0.22*	0.07	0.03*	0.02	0.06*	0.06	0.04*
T22	22				−1.60	0.07	−3.33	0.14	−4.95	0.20	−6.65	0.28	0.07	0.01	0.02	0.00	0.05	0.03

* 2SE on the average of the n measurements is below the 2SD RM 1 value, 2SD RM 1 value is reported (see Part 2.2).
[a] Net evaporation flux are calculated using a 20 cm^2 surface.
[b] Number of measurements.
[c] $\Delta^{199,200,201}$Hg′ are calculated relative to kinetic MDF process.
[d] T22-A sample: weight Hg 50 g, surface 3 cm^2; T22-B sample: weight Hg 250 g, surface 20 cm^2.
[e] ^{204}Hg isotope was monitored using a dynamic collection scheme, see Section 2.3.

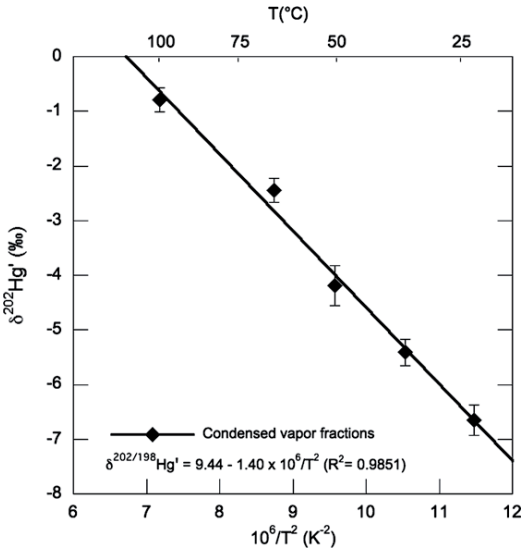

Fig. 4. The Hg isotopic composition of evaporated fractions (dynamic mode) between 22 and 100 °C are plotted against the temperature of evaporation $10^6/T^2$ (K) (Table 4). The linear relationship shows that the Hg isotopic fractionation during dynamic evaporation is strongly dependent on temperature (black line).

Vapor condensed fractions collected during this second set of experiments were also enriched in the lighter Hg isotopes. At 22 °C $\delta^{202}Hg' = -6.65 \pm 0.28‰$ (2SE; $n = 5$), and as the temperature increased, the vapor became increasingly less enriched in the lighter isotopes reaching a $\delta^{202}Hg'$ of $-0.79 \pm 0.22‰$ (2SE; $n = 2$) at 100 °C. Linearized $\delta^{202}Hg'$ are plotted versus $10^6/T^2$ in Fig. 4. Extrapolation of the linear relationship constrains the temperature where isotopic fractionation tends towards zero at ca. 115 °C. Alternatively, such a relationship with temperature could be related to progressive condensation of vapor Hg on its way to the cold trap, like suspected for some experiments conducted at 22 °C. Indeed, Brönsted and Mulliken experiments used a cold surface only 3 cm above the evaporating liquid Hg in order to prevent any loses on the way. Based on their density results, we calculated no significant change in alpha values from 40 to 80 °C. On the other hand, the fact that the isotopic composition of vapor Hg from the majority of our 22 °C experiments are reproducible and fits the evolution curve in a Rayleigh diagram (Fig. 3), along with the very good fit of $\delta^{202}Hg'$ with temperature, suggests that there might be a variation of $\alpha_{liq-vap}$ with the temperature of Hg evaporation in our set of experiments.

3.3. Non-mass-dependent fractionation

Fig. 5 illustrates a Hg three-isotope diagram, on which mass-dependent equilibrium fractionation lines between linearized $\delta^{202}Hg'$ (abscissa) and $\delta^{199}Hg'$, $\delta^{200}Hg'$, $\delta^{201}Hg'$ (ordinates) have been traced and equilibrium evaporation data plotted. No deviation from the equilibrium mass-dependent fractionation line is reported for $\delta^{200}Hg'$, whereas $\delta^{199}Hg'$ and $\delta^{201}Hg'$ yield a small but significant deviation from the mass fractionation line.

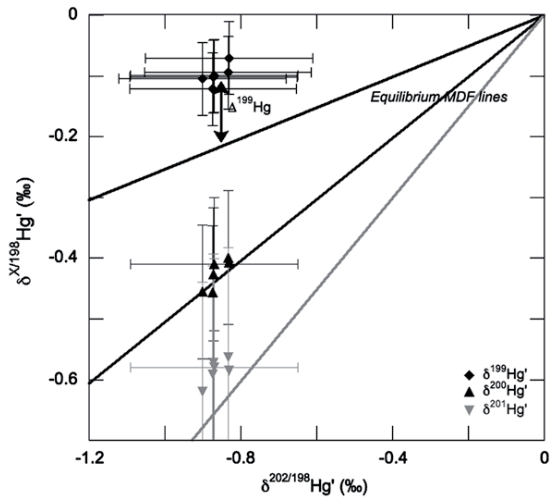

Fig. 5. A three-isotope diagram, where the isotopic composition of saturated Hg vapor from equilibrium evaporation experiments is represented as $\delta^{202}Hg'$ in abscissa against $\delta^{199}Hg'$, $\delta^{200}Hg'$ and $\delta^{201}Hg'$ in ordinates. Equilibrium MDF lines are reported (gray and black lines) for the three delta values. A significant deviation from the MDF lines is observed for ^{199}Hg and ^{201}Hg and may be quantified using $\Delta^{X}Hg'$ ($\Delta^{X}Hg' = \delta^{X}Hg'_{measured} - \beta^{Xvs202}_{Eq/Kin}\delta^{202}Hg'_{measured}$). Average $\Delta^{199}Hg'$ and $\Delta^{201}Hg'$ for 6 independent equilibrium evaporation are, respectively, $0.12 \pm 0.04‰$ (2SD, $n = 6$) and $0.07 \pm 0.03‰$ (2SD, n = 6).

In order to quantify NMF, the resulting measurements should be treated as if mass dependent. Quantification of non-mass-dependent fractionation, e.g. $\Delta^{X}Hg'$ (‰) (see Fig. 5) is defined as the difference between the measured $\delta^{X}Hg'$ and the value of $\delta^{X}Hg'$ if fractionation was entirely mass dependent (kinetic or equilibrium). Expression of these capital delta values (Hulston and Thode, 1965; Young and Galy, 2004; Blum and Bergquist, 2007) for isotopes 199, 200 and 201 are given below:

$$\Delta^{199}Hg' = \delta^{199}Hg'_{measured} - \beta^{199vs202}_{Eq/Kin}\delta^{202}Hg'_{measured}$$

$$\Delta^{200}Hg' = \delta^{200}Hg'_{measured} - \beta^{200vs202}_{Eq/Kin}\delta^{202}Hg'_{measured}$$

$$\Delta^{201}Hg' = \delta^{201}Hg'_{measured} - \beta^{201vs202}_{Eq/Kin}\delta^{202}Hg'_{measured} \quad (17)$$

The β values used (equilibrium or kinetic) are given in Table 2. The analytical uncertainties on $\Delta^{199}Hg'$, $\Delta^{200}Hg'$ and $\Delta^{201}Hg'$ (0.03‰, 0.06‰ and 0.04‰, respectively, 2SD), were determined from long-term liquid Hg° reference material analysis as described in Section 2.2. This supports the fact that $\Delta^{199}Hg'$ and $\Delta^{201}Hg'$ measured here are significant (tenth of a permil) but much smaller than values reported for some natural samples such as fish tissues (few permil; Bergquist and Blum, 2007).

In order to verify that the observed deviations of odd Hg isotope ratios from the equilibrium MDF lines are not analytical artifacts, we investigated potential interferences. Neither $^{199}Hg^+$ nor $^{201}Hg^+$ have isobaric interferences from other stable isotopes, yet both have potential molecular interferences from $^{159}Tb^{40}Ar^+$, $^{183}W^{16}O^+$, $^{181}Ta^{18}O^+$, $^{185}Re^{14}N^+$, $^{198}Hg^1H^+$, $^{198}Pt^1H^+$, and

$^{161}Dy^{40}Ar^+$, $^{185}Re^{16}O^+$, $^{187}Os^{14}N^+$ $^{200}Hg^1H^+$, respectively. Signal intensities for Tb, Dy, W, Re, Os, Pt isotopes were monitored during sample and bracketing standard analysis and found to be insignificant (<0.0005 V). Since $SnCl_2$ rather than $NaBH_4$ is used for on-line Hg(II) reduction to Hg(0), no volatile metal hydrides are produced during cold vapor generation. Detailed $^{199}Hg^+$ and $^{201}Hg^+$ peak scans were made in both low and high mass resolution modes of the Neptune MC-ICP-MS in order to verify unexpected molecular interferences, but no evidence was observed of peak shoulders or deviations from flat peak tops. The reduction efficiency of the CV system was verified to be >99.5% efficient by analyzing the gas–liquid separator waste line for any remaining Hg(II). Finally $^{120}Sn^+$ was monitored regularly during sessions to monitor CV membrane failure and found to be <4 mV at all times, ruling out further exotic interferences such as $^{119}Sn^{40}Ar^{40}Ar^+$ as well as mass-dependent matrix effects on instrumental mass bias. Based on these tests, the absence of odd-isotope anomalies in the liquid Hg starting material, and the identical sample preparation and ensuing analysis matrix (Hg(II) in 5% HNO_3), we conclude that the observed odd-isotope anomalies in Fig. 5 are real and are a component of the equilibrium isotope effect. At this point a final, testable, criteria of quality can be postulated: if evaporation of liquid Hg results in an excess of the ^{199}Hg and ^{201}Hg isotopes in the vapor, then automatically the residual liquid should develop a deficit of the ^{199}Hg and ^{201}Hg isotopes.

Then, equilibrium evaporation experiments present $\Delta^{199}Hg'$ from +0.10‰ to +0.14‰ and $\Delta^{201}Hg'$ from +0.04‰ to +0.08‰ whereas $\Delta^{200}Hg'$ from −0.02 to +0.03‰ for each evaporation sample (Table 2). Isotopic fractionation measured as $\delta^{199}Hg'$ and $\delta^{201}Hg'$ indicates an excess of the two odd isotopes in the vapor phase ($\Delta^{199}Hg'$ and $\Delta^{201}Hg' > 0$) compared to MDF, whereas no isotopic anomalies were found for the ^{200}Hg isotope. The average $\Delta^{199}Hg'$ and $\Delta^{201}Hg'$ of saturated vapor relative to the liquid are 0.12 ± 0.03‰ (2SD, $n = 6$) and 0.07 ± 0.04‰, (2SD, $n = 6$), respectively.

Dynamic evaporation experiments conducted at 22 °C also present NMF (see Table 4). Again condensed vapor have $\Delta^{199}Hg'$ and $\Delta^{201}Hg' > 0$‰, (from 0.08‰ to 0.05‰ and from 0.06‰ to 0.03‰, respectively), indicating an excess of the two odd isotopes in the vapor phase compared to mass-dependent equilibrium isotope fractionation. The residual liquid Hg fractions have $\Delta^{199}Hg'$ and $\Delta^{201}Hg' < 0$‰, (from −0.12‰ to −0.02‰ and from −0.09‰ to −0.01‰, respectively), indicating a deficit in the odd isotopes. The above outlined quality criteria is therefore met with our dynamic experiments: counter anomalies are measured in the Hg vapor and its relative residual liquid Hg. Fig. 6 illustrates the evolution of $\Delta^{199}Hg'$ with decreasing f_{Hg} for residual liquid and evaporated fractions. Residual liquid fractions display a gradual increase in the (negative) magnitude of $\Delta^{199}Hg'$ with increasing f_{Hg}, suggesting that the more evaporation takes place, the larger the anomaly is. Despite the significantly positive $\Delta^{199}Hg'$ anomalies of the vapor phase (Fig. 6), the $\Delta^{199}Hg'$ values do not provide a pronounced trend with f_{Hg}. The set of $\Delta^{199}Hg'$ values for the dynamic experimental data can be modeled with Rayleigh isotope fractionation equations:

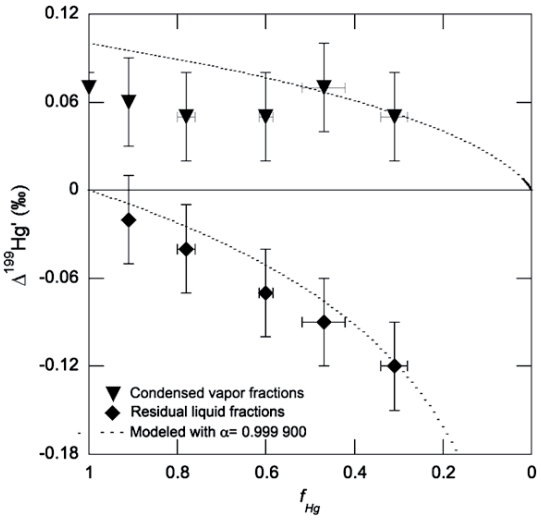

Fig. 6. A Rayleigh diagram reporting the evolution of $\Delta^{199}Hg'$ with the residual liquid fraction f_{Hg} for the dynamic evaporation experiments done at 22 °C. Residual liquid fractions display increasing anomalies with the ongoing evaporation. A Rayleigh fractionation behavior is modeled according to Eq. (7) with a liquid–vapor fractionation factor of $0.999\ 900 \pm 0.000\ 025$ (2SD) (gray dashed line). This value also fit the measured ^{201}Hg isotope anomalies.

$$\Delta^{199}Hg'_{res.liq} = 1000\left(f^{\left(\frac{1}{\alpha}-1\right)} - 1\right), \quad \Delta^{199}Hg'_{vap} = 1000\left(\frac{1-f^{\frac{1}{\alpha}}}{1-f} - 1\right) \tag{18}$$

A fitted Rayleigh fractionation factor between liquid and vapor of $0.999\ 900 \pm 0.000\ 025$ (2SD) for both $\Delta^{199}Hg'$ and $\Delta^{201}Hg'$ was obtained using the same procedure as described Section 3.2.

The variable temperature experiments present limited NMF (see Table 4) in the ranges of $\Delta^{199}Hg'$ of +0.02‰ to +0.07‰, but do not show a temperature dependency as observed for $\delta^{202}Hg'$ (Fig. 4). The ^{204}Hg isotope was monitored using a dynamic collection scheme (see Section 2.2) for sample T100 (Table 2 and Fig. 7). Calculation of $\Delta^{204}Hg'$ did not reveal isotopic anomalies.

4. DISCUSSION

In the following, evaporation and isotope fractionation processes are discussed to explain isotopic fractionation reported during equilibrium and dynamic evaporation experiments of liquid mercury. In the first part, we will discuss the extent of MDF using the $\delta^{202}Hg'$ and in the second part the NMF using the odd ^{199}Hg and ^{201}Hg isotopes.

4.1. Liquid–vapor isotope fractionation factors

Under equilibrium conditions, evaporation and condensation fluxes are equal and no physical kinetic isotopic fractionation should occur between liquid and vapor (Dauphas and Rouxel, 2006). Indeed, equilibrium may be reached in a

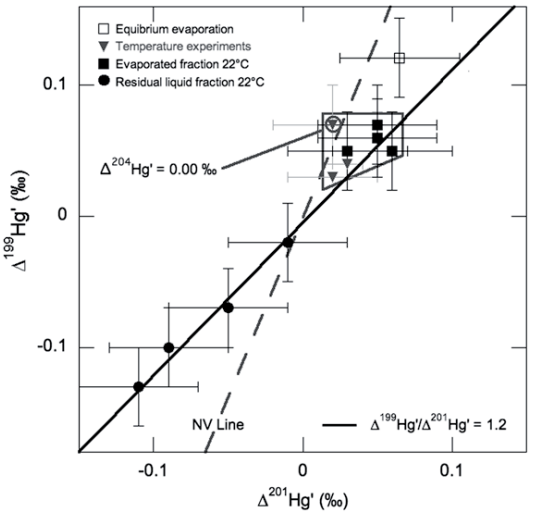

Fig. 7. Isotopic anomalies $\Delta^{199}Hg'$ versus $\Delta^{201}Hg'$ diagram into which data obtained for equilibrium and dynamic evaporation experiments were reported. Nuclear volume fractionation line (gray dashed line) using a slope of 2.47 (see text) is reported. Coordinates point (0;0) represents in this diagram MDF process. The compositions of residual liquid fractions from dynamic evaporation define a straight line with a slope $\Delta^{199}Hg'/\Delta^{201}Hg' = 1.2 \pm 0.4$ (2SD, X-Y isoplot regression) (Black line) (one outsider data point was rejected from calculations, see Table 4). Condensed vapor fractions are scattered between nuclear volume fractionation line and the residual liquid fractions NMF line. One vapor data point (circled) falling on the nuclear volume line was measured for its $\delta^{204}Hg$ value and did not revealed ^{204}Hg isotopic anomaly relative to MDF ($\Delta^{204}Hg' = 0‰$).

closed liquid–vapor system after continual exchange between the two Hg phases so that the evaporation–condensation reaction rapidly goes back and forth and total Hg $J_{evap.} = J_{cond.}$ (net evaporation = 0). The coherence of our results from many independent experiments suggests that chemical equilibrium was achieved ($P_i = P_{sat}$), but that an isotopic fractionation ($\alpha^{Eq}_{liq-vap} = 1.000\ 86 \pm 0.000\ 22$ on $^{202/198}Hg$) between the liquid and vapor was measured. Although Richter (2004) proposed that such a situation may result from a slight difference in the saturated vapor pressure from one isotope to another, a major question in the understanding of isotopic fractionation during evaporation–condensation processes is how does a system reach equilibrium from its initial conditions? When the vapor pressure is building up above liquid Hg, the first Hg fractions to evaporate must be affected by nearly pure kinetic fractionation ($\delta^{202}Hg$ of the vapor $\sim -10.1‰$ relative to the liquid). Approaching the saturated vapor pressure, condensation of vapor Hg^0 starts to progressively attain the situation where $J_{evap.} = J_{cond.}$ at equilibrium. In order to bring back the isotopic composition of the vapor from $-10‰$ towards $-0.86‰$ (as measured here at equilibrium), $(J_1/J_2)_{evap.}$ must be different from $(J_1/J_2)_{cond.}$ (see Eq. (5)) until total fluxes $J_{evap.} = J_{cond.}$. At this point, $(J_1/J_2)_{evap.} = (J_1/J_2)_{cond.}$ otherwise the isotopic composition of the vapor will continuously evolve and never reach an "equilibrium" value.

In an open system like the one represented by the dynamic evaporation under vacuum, one can imagine that the evaporation–condensation reaction operates within a thin layer at the liquid–vapor interface and that Hg° vapor can escape and condense further away, sampling the isotopic composition of vapor within the interface layer as proposed to explain Cd isotope fractionation during evaporation (Wombacher et al., 2004). The apparent overall isotopic fractionation during evaporation will then depend on the evaporation–condensation fluxes for all isotopes between the liquid and the vapor within the interface layer ($J_{evap.}$ and $J_{cond.}$), and the flux of vapor Hg escaping from the layer (J_{escape}), the latter will regulate the $J_{evap.}$ and $J_{cond.}$ equilibrium (Fig. 8). A pure kinetic fractionation

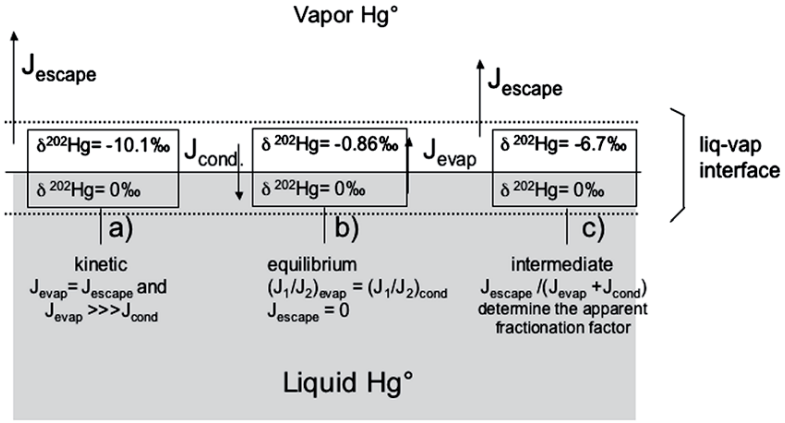

Fig. 8. Scheme of the conceptual model relating evaporation ($J_{evap.}$) condensation ($J_{cond.}$) and escape (J_{escape}) fluxes to liquid–vapor isotopic fractionation at the liquid–vapor interface layer. Conditions changing fluxes relationship will control the apparent liquid–vapor fractionation factor. Evaporation will proceed with $J_{evap.}$ only so that the first vapor produced will be strictly affected by kinetic fractionation (a). The system will move towards equilibrium for which evaporation and back condensation fluxes will be equal because no Hg escapes from the system (b). Our dynamic evaporation experiments are represented by an intermediate situation (c) where the apparent liquid–vapor fractionation factor will depend on an equilibrium between $J_{evap.}$, $J_{cond.}$ and J_{escape}.

would then be recorded when (J_{escape}) >> ($J_{evap.}$ and $J_{cond.}$), a free evaporation situation, whereas equilibrium conditions will be reached when (J_{escape}) << ($J_{evap.}$ and $J_{cond.}$), in other words when (J_{escape}) = 0, a closed system. In this conceptual system, the (J_{escape})/($J_{evap.} + J_{cond.}$) ratio will determine the apparent isotopic fractionation during evaporation. Indeed, the liquid–vapor isotopic fractionation factor under dynamic evaporation measured in this study, as well as in historical studies, is smaller than the theoretically expected value for pure kinetic. This situation is also abundantly reported in the literature (e.g. Davis et al., 1990; Wang et al., 2001; Richter et al., 2002, 2007; Dauphas et al. 2004). For example, Wombacher et al. (2004) undertook a moderate temperature (180 °C) evaporation of molten Cd under vacuum for which liquid–vapor fractionation factor was 40–50% smaller than the theoretical expected value (Wombacher et al., 2008) similar to what was reported by Richter et al. (2002) for high temperature Mg evaporation. We report here, a fractionation factor 40–50% smaller than the expected value calculated from Eq. (7): $\alpha^{total}_{202/198} = \alpha^{Eq}_{202/198}\sqrt{\frac{m_{202}}{m_{198}}} = 1.00086 \times \sqrt{\frac{201.970632}{197.96676}} = 1.0109$.

In our various kinetic experiments at 22 °C, the net evaporation flux J is highly variable according to the amount of starting liquid Hg. Small droplets evaporated at a flux varying between 1.4×10^{-6} and 8.3×10^{-6} mol cm^{-2} s^{-1} (Table 4), whereas lower fluxes of 0.2–0.5 $\times 10^{-6}$ mol cm^{-2} s^{-1} were recorded for larger amounts of liquids having 20 and 3 cm^2 of surface to evaporate, respectively (Table 5). Finding a similar liquid–vapor fractionation factor of 1.0067 for all the experiments at 22 °C, we suggest that both (J_{escape})/($J_{evap.}$) and J_1/J_2 at evaporation and condensation at the liquid–vapor interface are equal and constant at 22 °C, independently of the absolute fluxes values. This also indicates that the liquid mercury reservoir was well mixed during the evaporation process (Wang et al., 2001). This instantaneous homogenization prevented evaporation from diffusion-controlled process (Ozawa and Nagahara, 2001), which would lead to an isotopic stratification of the liquid surface (Wombacher et al., 2004).

Experiments conducted at higher temperature show that the isotopic fractionation of Hg during evaporation is smaller and that there is a strong relationship with the temperature (Fig. 4). The saturated vapor pressure is a power function of temperature such that the partial pressure above the liquid should also have increased with temperature. However, Hg vapor probably never reached the saturated pressure in the whole assembly because of the cold trap. Furthermore, the net evaporation flux increased with temperature (Table 5), an inverse situation from the one predicted by Eq. (2) in a system reaching equilibrium. This suggests that conditions changed within the interface layer, such as the (J_{escape})/($J_{evap.}$) ratio. Raising the temperature of the system certainly affects the kinetics of phase transformations so that equilibrium is more rapidly reached in the liquid–vapor interface layer. Because Hg extracted from the layer by J_{escape} reflects the isotopic composition of the vapor within the layer, this would explain why the apparent liquid–vapor isotopic fractionation changes with temperature.

4.2. Evaporation processes and non-mass-dependent fractionations

We report here that vapor above the liquid Hg sampled at chemical equilibrium between 0 and 22 °C (equivalent to saturated vapor) is isotopically fractionated relative to liquid. In this work, is reported a significant fractionation ($\alpha_{Eq} = 1.000\ 86 \pm 0.000\ 05$) between Hg° vapor in equilibrium with infinite liquid Hg reservoir. Isotopic fractionation is not mass dependent, at least for the odd 199 and 201 Hg isotopes.

In order to potentially discriminate nuclear volume fractionation from magnetic isotope effect as a cause of NMF, the ratio of anomalies $\Delta^{199}Hg'/\Delta^{201}Hg'$ are of interest. Indeed, in a plot $\Delta^{199}Hg'$ versus $\Delta^{201}Hg'$, where $\Delta^{199}Hg' = 0$ and $\Delta^{201}Hg' = 0$ coordinates represent MDF, we can define a nuclear volume fractionation line according to fractionation laws and β values described in Section 2.4 and listed in Table 2, leading to a slope of 2.47 based on the Hahn et al. (1979) $\langle r^2 \rangle$ values (Fig. 7). Given the sensitivity of this slope to $\langle r^2 \rangle$ values, caution should be taken in attributing an exact slope value. Recent work by Bergquist and Blum (2007) on inorganic Hg(II) and methyl-Hg photoreduction revealed a different evolution of 199 and 201 Hg isotope anomalies. In a $\Delta^{199}Hg'$ versus $\Delta^{201}Hg'$ diagram Hg(II) and MeHg photoreduction define slopes of 1.00 and 1.36 (±0.02, 2SE), respectively. Based on the photochemical nature of their experiments, likely involving Hg radical intermediates, Bergquist and Blum (2007) suggested the MIE to be the responsible non-mass-dependent isotope fractionation mechanism. Ghosh et al. (2008) recently suggested that the MIE induces a $\Delta^{199}Hg'/\Delta^{201}Hg'$ slope of 0.90 defined by the ratio of the respective ^{199}Hg and ^{201}Hg nuclear magnetic moments of +0.5029 and −0.5602 μ_B. However, no theoretical framework exists for prediction of MIE that would justify such an educated guess.

The average $\Delta^{199}Hg'$ and $\Delta^{201}Hg'$ for equilibrium evaporation experiments plotted in Fig. 7 is similar to the nuclear volume fractionation line within the analytical uncertainty ($\Delta^{199}Hg'/\Delta^{201}Hg' = 2.0 \pm 0.6$; 2SE, $n = 6$). Since the magnetic isotope effect is a kinetic phenomena (Buchachenko, 2001; Bergquist and Blum, 2007), we suggest therefore that Hg isotope fractionation between liquid Hg and vapor Hg under equilibrium conditions is caused by nuclear volume fractionation in addition to mass fractionation.

Theoretical work by Bigeleisen (1996) and Schauble (2007) indicates that nuclear volume fractionation can occur if and only if the electronic configuration between reactants and products is modified. In our case, equilibrium evaporation involves a priori no distinction between the electronic configuration of liquid metallic mercury (Hg^0: [Xe]4f^{14}5d^{10}6s^2) and monoatomic elemental mercury vapor (Hg^0: [Xe]4f^{14}5d^{10}6s^2). However, in metallic bonding valence electrons in the 6s orbital are shared and one can straightforwardly rationalize that the odd ^{199}Hg and ^{201}Hg isotopes with their small nuclear volume, and high nuclear charge density tend to share their valence electrons less than the ^{198}Hg, ^{200}Hg and ^{202}Hg isotopes. Consequently, ^{199}Hg and ^{201}Hg have weaker metallic bonds and

thus a higher vapor pressure, which will tend to enrich them in the vapor, in accordance with our observations.

Dynamic evaporations conducted at 22 °C also showed NMF. $\Delta^{199}Hg'$ and $\Delta^{201}Hg'$ follow Rayleigh behavior (Fig. 6) with a common fractionation factor of 0.999 900 ± 0.000 025 (2SD). As the evaporation takes place, the residual liquid fractions are depleted in ^{199}Hg and ^{201}Hg isotopes relative to MDF and the $\Delta^{199}Hg'/\Delta^{201}Hg'$ ratios (Fig. 7) are close to unity (1.2 ± 0.4 (2SD)), significantly different from the slope of 2.47 involved in nuclear volume fractionation but in the range of the estimated relationship for magnetic isotope effects. However, according to the theory, the absence of known Hg radical intermediates in liquid Hg evaporation would preclude any magnetic isotope effect. Our experimental results suggest that either magnetic isotope effects may take place without radical chemistry or that another unknown process may lead to NMF of odd Hg isotopes resulting in a $\Delta^{199}Hg'/\Delta^{201}Hg'$ relationship of ca. 1.

Isotopic anomalies measured in vapor condensed fractions collected at 22 °C from the small liquid Hg droplet and vapor condensed fractions collected between 22 and 100 °C from the large liquid mercury reservoir are also plotted in Fig. 7 and show a scattering between the nuclear volume fractionation line and the residual liquid fractions NMF line. These anomalies are very small and, according to their relatively large uncertainties, do not discriminate potential NMF processes. In any case, the fact that negative anomalies in the residual liquid fractions are balanced by positive anomalies in the condensed vapor strongly supports that NMF occurred during liquid Hg dynamic evaporation.

5. CONCLUSION

Liquid mercury evaporation experiments, under equilibrium and dynamic conditions, led to significant isotopic fractionation governed by mass-dependent and non-mass-dependent fractionation processes.

Mercury vapor sampled at chemical equilibrium with Hg liquid at various temperatures from 0 to 22 °C were fractionated from the starting liquid for six independent experiments (vapor $\delta^{202}Hg' = 0.86 \pm 0.22‰$). This correspond to a constant liquid–vapor fractionation factor ($\alpha_{202/198}$) between liquid and vapor of 1.000 86 ± 0.000 22 (2SD, $n = 6$) for this temperature range.

The 22 °C dynamic evaporations experiments displayed a Rayleigh distillation behavior with liquid–vapor $\alpha_{202/198} = 1.0067 \pm 0.0011$ (2SD) calculated from both residual and condensed vapor fractions. Our results confirm historical data set (1920s) from Brönsted, Mulliken and coworkers on mercury isotopes separation using evaporation experiments, for which recalculated $\delta^{202}Hg'$ showed a liquid–vapor $\alpha_{202/198}$ of 1.0076 ± 0.0017 (2SD). Our experimental liquid–vapor $\alpha_{202/198}$ is 40% lower than the total expected $\alpha_{202/198}$ value ($\alpha_{Eq}\alpha_{Kin} = 1.0109$) in open system, a situation widely reported in the literature. A conceptual evaporation model including back condensation within a thin layer at the liquid–vapor interface was used to explain this discrepancy. In such model, the isotopic fractionation measured for the condensed vapor represents the isotopic composition of the vapor within the layer. The $\delta^{202}Hg'$ of condensed vapor fractions in the 22–100 °C range experiments showed a negative linear relationship with $10^6/T^2$, explained by increasing the kinetic of equilibrium reactions within the layer with the increase in temperature.

Evaporation experiments also resulted in non-mass-dependent fractionation of odd ^{199}Hg and ^{201}Hg isotopes, expressed as $\Delta^{199}Hg'$ and $\Delta^{201}Hg'$, the deviation in ‰ from the mass fractionation relationship with even isotopes. Liquid–vapor equilibrium yielded $\Delta^{199}Hg'/\Delta^{201}Hg'$ relationship of 2.0 ± 0.6 (2SE, $n = 6$), similar to the ratio predicted for nuclear field shift effects ($\Delta^{199}Hg/\Delta^{201}Hg \approx 2.47$). Dynamic evaporation experiments led to negative anomalies in the residual liquid fraction that are balanced by positive anomalies in condensed vapor. The $\Delta^{199}Hg'/\Delta^{201}Hg'$ measured in the residual liquid for the 22 °C dynamic evaporation experiments is similar to unity (1.2 ± 0.4, 2SD), which suggest that magnetic isotope effect may have occurred without radical chemistry or an unknown NMF process on odd isotopes operated during liquid mercury evaporation.

ACKNOWLEDGMENTS

We thank Christian France-Lanord and Caroline Guilmette (CRPG-stable isotopes lab) for evaporation assistance, Luc Marin and Jitka Lhomme (CRPG-chemistry lab) for their technical support and Remy Freydier for analytical assistance on the LMTG Neptune. Two anonymous reviewers, Edwin Schauble and the associated editor James Farquhar are thanked for their constructive comments. CRPG contribution N°1990.

APPENDIX A

Table A1. Summary of historical experimental data on Hg^0(liq) evaporation and condensation by Brönsted, and Harkins and coworkers (REFS). Original experimental codes are given, as well as new codes (exp#, column 1) that are referred to in the main text. Original data are shown in bold type face; recalculated parameters are shown in plain type face. *Abbreviations:* T, temperature; V, volume; f, fraction; evap., evaporate, res., residue; $d(\rho)$, change in density in ppm.

Exp#	Original exp#	Publication	Description	T (°C)	Liquid Hg starting material	Cut[d]	Efficiency %	Starting V(A) (cm^3)	f (A)	$1-f$ (B)	Evap. (A) (cm^3)	Res. (B) (cm^3)	$d(\rho)$ in B (ppm)	$d(\rho)$ in A (ppm)	Relative $d(\rho)$ in B	relative $d(\rho)$ in A	δ^{202}Hg. res.	δ^{202}Hg evap.
0			Starting Hg(liq)														0.00	
1		Brönsted'20	Evaporation		0		75[a]	**40**	0.86	0.14	5.7	34.3	**−20**		0.999980		1.16	−6.97
2		Brönsted'20	Evaporation		0		75[a]	**40**	0.25	0.75	30.0	10.0		**31**		1.000031	10.50	−3.50
3	**1**	Mulliken'22	Evaporation	**40**	0	**1.03**	**93**	**40**	0.97	0.03	1.2	38.8	**−29**		0.999971		0.22	−7.42
4	**2**	Mulliken'22	Evaporation	**40**	0	**2.22**	**93**	**40**	0.45	0.55	22.0	18.0	**−20**	**18**	0.999980	1.000018	6.03	−4.94
5	**3**	Mulliken'22	Evaporation	**85**	0	**1.57**	**83**	**40**	0.64	0.36	14.5	25.5	**−20**	**9**	0.999980	1.000009	3.40	−5.97
6	**4**	Mulliken'22	Sequential evaporation	**85**	0	**2.0**	**80**	**40**	0.50	0.50	20.0	20.0					5.24	−5.24
7	**4**		Sequential evaporation	**85**	Exp#6	**2.0**	**80**	**20**	0.50	0.50	10.0	10.0					−0.03	−10.44
8	**4**		Sequential evaporation	**85**	Exp#7	**2.0**	**80**	**10**	0.50	0.50	5.0	5.0					−5.26	−15.62
9	**4**		Sequential evaporation	**85**	Exp#8	**2.0**[b]	**80**	**5**	0.50	0.50	2.5	2.5	**−64**		0.999936		−10.47	−20.78
10	**5**	Mulliken'22	Sequential evaporation		0	**22.5**[c]	**80**	**40**	0.04	0.96	38.2	1.8		**69**		1.000069	23.73	−1.10
11	**6**	Mulliken'22	Full distillation		0	14.2	**6**	**85**	0.07	0.93	79.0	6.0	**−1.5**	**3.5**	0.999999	1.000004	−0.02	−9.64
12	**7**	Mulliken'22	Full distillation		0	**11.9**	**10**	**85**	0.08	0.92	77.9	7.1		**5.0**		1.000005	−4.85	−14.42
13	**8**	Mulliken'22	Full distillation		0	**14.2**	**10**	**85**	0.07	0.93	79.0	6.0	**−1.5**		0.999999		−9.66	−19.18
14	**8**	Mulliken'22	Full distillation		0	**13.0**	**10**	**85**	0.08	0.92	78.5	6.5		**7.2**		1.000007	21.88	−1.02
Brönsted'21 Table 1																		
15	**R1**	Brönsted'21	Evaporation		0			**2704**	0.76	0.24	**642**	**2062**			**0.999977**		2.04	−6.56
16	**R2**	Brönsted'21	Evaporation		0			2062	0.59	0.41	**461.0**	**1601**				**1.000016**	3.96	−5.74
17	**R3**	Brönsted'21	Evaporation		0			1603	0.47	0.53	**320.0**	**1283**					5.63	−5.08
18	**R4**	Brönsted'21	Evaporation		0			1273	0.38	0.62	**243.0**	**1030**				**1.000024**	7.30	−4.49
19	**R5**	Brönsted'21	Evaporation		0			1026	0.29	0.71	**235.0**	**791**					9.30	−3.85
20	**R6**	Brönsted'21	Evaporation		0			787	0.22	0.78	**202.0**	**585**				**1.000034**	11.60	−3.20
21	**R7**	Brönsted'21	Evaporation		0			583	0.18	0.82	**94.0**	**489**					12.97	−2.86
22	**R8**	Brönsted'21	Evaporation		0			497	0.14	0.86	**115.0**	**382**				**1.000053**	14.85	−2.44
23	**R9**	Brönsted'21	Evaporation		0			373	0.10	0.90	**105.0**	**268**					17.56	−1.93
24	**R10**	Brönsted'21	Evaporation		0			267	0.07	0.93	**82.0**	**185**					20.41	−1.50
25	**R11**	Brönsted'21	Evaporation		0			185	0.06	0.94	**35.0**	**150**					22.02	−1.29
26	**R12**	Brönsted'21	Evaporation		0			150	0.05	0.95	**22.0**	**128**				**1.000079**	23.24	−1.16
27	**R13**	Brönsted'21	Evaporation		0			129	0.02	0.98	**87.0**	**42**					31.87	−0.50
28	**R14**	Brönsted'21	Evaporation		0			41.8	0.00	1.00	**31.5**	**10.3**				**1.000134**	42.85	−0.16
29	**R15**	Brönsted'21	Evaporation		0			10.3	0.00	1.00	**4.8**	**5.5**				**1.000153**	47.79	−0.10
30	**R16**	Brönsted'21	Evaporation		0			5.5	0.00	1.00	**4.4**	**1.1**					60.57	−0.02
31	**R17**	Brönsted'21	Evaporation		0			1	0.00	1.00	**0.5**	**0.5**					66.89	−0.01

32	**R18**	Brönsted'21	Evaporation	0	0.5	0.00	1.00	**0.3**	**0.2**			**1.000230**	74.28	−0.01
33	**R1D1**	Brönsted'21 R1D1	Condensate	Evaporation	exp#29	2062	0.59	0.41	**461.0**	**1601**		**0.999989**	3.96	−3.71
34	**R12D1**	Brönsted'21 R12D1	Condensate	Evaporation	R27	129	0.02	0.98	**87.0**	**42**		**1.000060**	31.87	22.73
35	**R13D1**	Brönsted'21 R13D1	Condensate	evaporation	R28	41.8	0.00	1.00	**31.5**	**10.3**		**1.000090**	42.85	31.70
Brönsted'21 Table 2														
36	**D1R1 and D2**	Brönsted'21		Sequential evaporation	C36	626	0.754	0.246	**154**	**472**		**0.999953**	**0.999979**	−4.45	−13.05
37	**D2R1 and D3**	Brönsted'21		Sequential evaporation	C37	151	0.669	0.331	**50**	**101**		**0.999933**	**0.999961**	−10.05	−19.10
38	**D3R1 and D4**	Brönsted'21		Sequential evaporation	C38	49	0.724	0.276	**13.5**	**36**		**0.999911**	**0.999941**	−16.71	−25.37
39	**D4R1 and D5**	Brönsted'21		Sequential evaporation	C39	13.3	0.752	0.248	**3.3**	**10**		**0.999881**	**0.999914**	−23.27	−31.72

[a]An efficiency of 75% for Brönsted and von Hevesy's (1920) data was assumed by Mulliken and Harkins (1922).
[b]Four successive cuts[d] of 2 give a total cut of 16.
[c]Mulliken and Harkins cite an approximate cut of 20–25. We used the average of 22.5 in our fitting and simulation procedures.
[d]The cut of an experiment is defined as the residual Hg(liq) volume over the starting Hg(liq) volume, $V(0)/V(B)$ (Mulliken and Harkins, 1922).

REFERENCES

Angeli I. (2004) A consistent set of nuclear rms charge radii: properties of the radius surface R (N, Z). *Atom. Data Nucl. Data Tables* **87**, 185–206.

Bergquist B. A. and Blum J. D. (2007) Mass-dependent and -independent fractionation of Hg isotopes by photoreduction in aquatic systems. *Science* **318**, 417–420.

Bigeleisen J. (1949) The relative reaction velocities of isotopic molecules. *J. Chem. Phys.* **17**, 675–678.

Bigeleisen J. (1996) Nuclear size and shape effects in chemical reactions. Isotope chemistry of the heavy elements. *J. Am. Chem. Soc.* **118**, 3676–3680.

Biswas A., Blum J. D. and Bergquist B. A. (2008) Natural mercury isotope variation in coal deposits and organic soils. *Environ. Sci. Tech.* **404**, 129–138.

Blum J. D. and Bergquist B. A. (2007) Reporting of variations in the natural isotopic composition of mercury. *Anal. Bioanal. Chem.* **388**, 353–359.

Brönsted J. N. and von Hevesy G. (1920) The separation of the isotopes of mercury. *Nature* **106**, 144.

Brönsted J. N. and von Hevesy G. (1921) Uber die Trennung der Isotopen des Quecksilbers. *Zeitschrift fur Physikalische Chemie* **99**, 189–206.

Buchachenko A. L., Galimov E. M. and Ershov V. V. (1976) Isotopic enrichment induced by magnetic-interactions in chemical-reactions. *Dokl. Akad. Nauk SSSR* **228**, 379–382.

Buchachenko A. L. (1995) MIE versus CIE – comparative analysis of magnetic and classical isotope effects. *Chem. Rev.* **95**, 2507–2528.

Buchachenko A. L. (2000) Recent advances in spin chemistry. *Pure Appl. Chem.* **72**, 2243–2258.

Buchachenko A. L. (2001) Magnetic isotope effect: nuclear spin control of chemical reactions. *J. Phys. Chem. A* **105**, 9995–10011.

Buchachenko A. L., Kouznetsov D. A. and Shishkov A. V. (2004) Spin biochemistry: magnetic isotope effect in the reaction of creatine kinase with CH_3HgCl. *J. Phys. Chem. A* **108**, 707–710.

Buchachenko A. L., Ivanov V. L., Roznyatovskii V. A., Artamkina G. A., Vorob'ev A. K. and Ustynyuk Y. A. (2007) Magnetic isotope effect for mercury nuclei in photolysis of bis(*p*-trifluoromethylbenzyl)mercury. *Doklady Phys. Chem.* **413**, 39–41.

Dauphas N., Janney P. E., Mendybaev R. A., Wadhwa M., Richter F. M., Davis A. M., van Zuilen M., Hines R. and Foley C. N. (2004) Chromatographic separation and multicollection-ICPMS analysis of iron. Investigating mass-dependent and -independent isotope effects. *Anal. Chem.* **76**, 5855–5863.

Dauphas N. and Rouxel O. (2006) Mass spectrometry and natural variations of iron isotopes. *Mass Spectrom. Rev.* **25**, 515–550.

Davis A. M., Hashimoto A., Clayton R. N. and Mayeda T. K. (1990) Isotope mass fractionation during evaporation of $MgSiO_4$. *Nature* **347**, 655–658.

Epov V. N., Rodriguez-Gonzalez P., Sonke J. E., Tessier E., Amouroux D., Bourgoin L. M. and Donard O. F. X. (2008) Simultaneous determination of species-specific isotopic composition of Hg by gas chromatography coupled to multicollector ICPMS. *Anal. Chem.* **80**, 3530–3538.

Foucher D. and Hintelmann H. (2006) High-precision measurement of mercury isotope ratios in sediments using cold-vapor generation multi-collector inductively coupled plasma mass spectrometry. *Anal. Bioanal. Chem.* **384**, 1470–1478.

Goldstein S. L., Deines P., Oelkers E. H., Rudnick R. L. and Walter L. M. (2003) Standards for publication of isotope ratio and chemical data in Chemical Geology. *Chem. Geol.* **202**, 1–4.

Ghosh S., Xu Y. F., Humayun M. and Odom L. (2008) Mass-independent fractionation of mercury isotopes in the environment. *Geochem. Geophys. Geosyst.* **9**.

Hahn A. A., Miller J. P., Powers R. J., Zehnder A., Rushton A. M., Welsh R. E., Kunselman A. R., Roberson P. and Walter H. K. (1979) An experimental study of muonic X-Ray transitions in mercury isotopes. *Nuclear Physics* **A314**, 361–386.

Hintelmann H. and Lu S. Y. (2003) High precision isotope ratio measurements of mercury isotopes in cinnabar ores using multi-collector inductively coupled plasma mass spectrometry. *Analyst* **128**, 635–639.

Hoefs J. (1987) *Stable Isotope Geochemistry*, third ed. Springer-Verlag, Berlin, 241 pp.

Hulston J. R. and Thode H. G. (1965) Variations in the S33, S34, and S36 contents of meteorites and their relation to chemical and nuclear effects. *J. Geophys. Res.* **70**, 3475–3484.

Jackson T. A., Muir D. C. G. and Warwick F. V. (2004) Historical variations in the stable isotope composition of mercury in arctic lake sediments. *Environ. Sci. Tech.* **38**, 2813–2821.

Jackson T. A., Whittle D. M., Evans M. S. and Muir D. C. G. (2008) Evidence for mass-independent and mass-dependent fractionation of the stable isotopes of mercury by natural processes in aquatic ecosystems. *Appl. Geochem.* **23**, 547–571.

Jackson T. A., Whittle D. M., Evans M. S. and Muir D. C. G. (2006) Mass-independent fractionation of Hg isotopes by biological processes. *Geochim. Cosmochim. Acta* **70**, A284–A284.

Klaue, B., Kesler, S. E. and Blum, J. D. (2000). Investigation of the natural fractionation of stable mercury isotopes by ICPMS. In *International Conference on Heavy Metals in the Environment*. Ann Arbor, MI, USA.

Kritee K., Blum J. D., Johnson M. W., Bergquist B. A. and Barkay T. (2007) Mercury stable isotope fractionation during reduction of Hg(II) to Hg(0) by mercury resistant microorganisms. *Environ. Sci. Tech.* **41**, 1889–1895.

Lauretta D. S., Klaue B., Blum J. D. and Buseck P. R. (2001) Mercury abundances and isotopic compositions in the Murchison (CM) and Allende (CV) carbonaceous chondrites. *Geochim. Cosmochim. Acta* **65**, 2807–2818.

Lohman K., Seigneur C., Gustin M. and Lindberg S. (2008) Sensitivity of the global atmospheric cycle of mercury to emissions. *Appl. Geochem.* **23**, 454–466.

Mulliken R. S. and Harkins W. D. (1922) The separation of isotopes. Theory of resolution of isotopic mixtures by diffusion and similar processes. Experimental separation of mercury by evaporation in a vacuum. *J. Am. Chem. Soc.* **44**, 37–65.

Nriagu J. and Becker C. (2003) Volcanic emissions of mercury to the atmosphere: global and regional inventories. *Sci. Tot. Environ.* **304**, 3–12.

Ozawa K. and Nagahara H. (2001) Chemical and isotopic fractionations by evaporation and their cosmochemical implications. *Geochim. Cosmochim. Acta* **65**, 2171–2199.

Pacyna E. G., Pacyna J. M., Fudala J., Strzelecka-Jastrzab E., Hlawiczka S. and Panasiuk D. (2006) Mercury emissions to the atmosphere from anthropogenic sources in Europe in 2000 and their scenarios until 2020. *Sci. Tot. Environ.* **370**, 147–156.

Pyle D. M. and Mather T. A. (2003) The importance of volcanic emissions for the global atmospheric mercury cycle. *Atmos. Environ.* **37**, 5115–5124.

Richter F. M. (2004) Timescales determining the degree of kinetic isotope fractionation by evaporation and condensation. *Geochim. Cosmochim. Acta* **68**, 4971–4992.

Richter F. M., Davis A. M., Ebel D. S. and Hashimoto A. (2002) Elemental and isotopic fractionation of Type B calcium-, aluminum-rich inclusions: experiments, theoretical considerations, and constraints on their thermal evolution. *Geochim. Cosmochim. Acta* **66**, 521–540.

Richter F. M., Janney P. E., Mendybaev R. A., Davis A. M. and Wadhwa M. (2007) Elemental and isotopic fractionation of Type BCAI-like liquids by evaporation. *Geochim. Cosmochim. Acta* **71**, 5544–5564.

Schauble E. A. (2004) Applying stable isotope fractionation theory to new systems. *Rev. Miner. Geochem.* **55**, 65–111.

Schauble E. A. (2007) Role of nuclear volume in driving equilibrium stable isotope fractionation of mercury, thallium, and other very heavy elements. *Geochim. Cosmochim. Acta* **71**, 2170–2189.

Selin, N. E., Jacob, D. J., Park, R. J., Yantosca, R. M., Strode, S., Jaegle, L. and Jaffe, D. (2007) Chemical cycling and deposition of atmospheric mercury: global constraints from observations. *J. Geophys. Res.-Atmos.* **112**.

Smith C. N., Kesler S. E., Klaue B. and Blum J. D. (2005) Mercury isotope fractionation in fossil hydrothermal systems. *Geology* **33**, 825–828.

Smith C. N., Kesler S. E., Blum J. D. and Rytuba J. J. (2008) Isotope geochemistry of mercury in source rocks, mineral deposits and spring deposits of the California Coast Ranges, USA. *Earth Planet. Sci. Lett.* **269**, 399–407.

Sonke J. E., Zambardi T. and Toutain J. P. (2008) Indirect gold trap-MC-ICP-MS coupling for Hg stable isotope analysis using a syringe injection interface. *J. Anal. Atom. Spectrom.* **23**, 569–573.

Turro N. J. and Kraeutler B. (1978) Magnetic isotope and magnetic field-effects on chemical-reactions – sunlight and soap for efficient separation of C-13 and C-12. *J. Am. Chem. Soc.* **100**, 7432–7434.

Turro N. J. (1993) Influence of nuclear spin on chemical, reactions: magnetic isotope and magnetic field effects (A Review). *Proc. Natl. Acad. Sci. USA* **80**, 609–621.

Urey H. C. (1947) The thermodynamic properties of isotopic substances. *J. Chem. Soc.*, 562–581.

Wang J. H., Davis A. M., Clayton R. N., Mayeda T. K. and Hashimoto A. (2001) Chemical and isotopic fractionation during the evaporation of the FeO–MgO–SiO_2–CaO–Al_2O_3–TiO_2 rare earth element melt system. *Geochim. Cosmochim. Acta* **65**, 479–494.

Weast R. C. (1999) *Handbook of Physics and Chemistry*. The Chemical Rubber Co., Cleveland.

Wombacher F., Rehkamper M. and Mezger K. (2004) Determination of the mass-dependence of cadmium isotope fractionation during evaporation. *Geochim. Cosmochim. Acta* **68**, 2349–2357.

Wombacher F., Rehkamper M., Mezger K., Bischoff A. and Münker C. (2008) Cadmium isotope cosmochemistry. *Geochim. Cosmochim. Acta* **72**, 646–667.

Xie Q. L., Lu S. Y., Evans D., Dillon P. and Hintelmann H. (2005) High precision Hg isotope analysis of environmental samples using gold trap-MC-ICP-MS. *J. Anal. At. Spectrom.* **20**, 515–522.

Young E. D. and Galy A. (2004) The isotope geochemistry and cosmochemistry of magnesium. *Rev. Miner. Geochem.* **55**, 197–230.

Young E. D., Galy A. and Nagahara H. (2002) Kinetic and equilibrium mass-dependent isotope fractionation laws in nature and their geochemical and cosmochemical significance. *Geochim. Cosmochim. Acta* **66**, 1095–1104.

Yu Y., Hewins R. H., Alexander C. M. O. and Wang J. (2003) Experimental study of evaporation and isotopic mass fraction-

ation of potassium in silicate melts. *Geochim. Cosmochim. Acta* **67**, 773–786.

Zambardi T., Sonke J. E., Toutain J-P., Sortino F. and Shinohara H. (2008) Mercury emissions and stable isotopic compositions at Vulcano Island (Italy). *Earth Planet. Sci. Lett.* **277**, 236–243.

Zheng W., Foucher D. and Hintelmann H. (2007) Mercury isotope fractionation during volatilization of Hg(0) from solution into the gas phase. *J. Anal. At. Spectrom.* **22**, 1097–1104.

Associate editor: James Farquhar

Mercury isotope fractionation during abiotic reduction by the hydroxysulfate green rust 2

Nicolas Estrade (1,2) *, Jean Carignan (1), Frédéric Jorand (3) and Olivier F.X. Donard (2)

(1) Centre de Recherche Pétrographique et Géochimique, Nancy Université, CNRS UPR 2300, BP 20, 54501 Vandoeuvre les Nancy, France.

(2) Institut Pluridisciplinaire de Recherche sur l'Environennement et les Matériaux, Laboratoire de Chimie-Analytique Bio-Inorganique et Environnement, Université de Pau et des Pays de l'Adour, CNRS UMR 5254, HELIOPARC, 64053 Pau, France.

(3) Laboratoire de Chimie Physique et Microbiologie pour l'Environnement, Nancy Université, LCPME UMR 7564 CNRS–Nancy-Université, 405 rue de Vandoeuvre, 54600 Villers-lès-Nancy, France.

*To whom correspondence should be addressed. e-mail: nestrade@crpg.cnrs-nancy.fr. Tel: +33 559407759

Key words: Mercury isotopic fractionation, abiotic reduction, green rust, mass dependent fractionation

Abstract

Hg(II) reduction isotope fractionation was investigated by using the abiotic Fe^{II}-Fe^{III} hydroxysalt green rust 2 (GR2), under anoxic conditions. Hg(II) was introduced to various green rust concentrations and fast reduction rates were observed for all experiments. The decreasing of remaining Hg(II) with time did not present regular rate of reduction. Transmission electronic microscopy measurements performed on GR2 after the reaction revealed mineral transformation (goethite and magnetite) and Hg^0 trapped onto the solid phase. These findings identified sub-sequent reactions in the reactor and suggest that Hg^0 is not easily evacuated from the system when solid suspension is present, even when bubbling. Isotope compositions of most Hg(II) fractions in the solution along the experiments presented enrichments in heavy isotopes compared to the starting material as the reaction proceeded, suggesting mass-dependent isotope fractionation. Some experiments reduced most of the initial Hg(II), which sometimes yielded an isotopic composition enriched in the lighter isotopes. This was attributed to a contribution of the Hg^0 produced and remaining in the suspension. Combined observations suggested that the $^{202/198}\alpha_{Hg(II)/Hg^\circ}$ has a minimum value of 1.0011. Abiotic reduction by green rusts display $^{202/198}\alpha_{Hg(II)/Hg^\circ}$ in the range of others mercury reduction processes (1.0005-1.002) documented.

Introduction

The global biogeochemical mercury (Hg) cycle is currently not well constrains because of many uncertainties regarding sources and sinks as well as secondary emission processes (Lindberg et al., 2007; Selin, 2009; Gustin and Jaffe, 2010). Mercury is one of those isotope systems that shows mass dependent (MDF) and mass independent fractionation (MIF). Some source-reservoirs and key reactions controlling the Hg biogeochemical cycle throughout its transport into the environment were specifically studied for documenting isotopic compositions and fractionations. This allowed to built a framework for Hg isotope geochemistry and thus discriminate sources, trace and apportion their contributions in various environmental reservoirs (e.g. Bergquist and Blum, 2007; Foucher and Hintelmann, 2009, Carignan et al., 2009; Estrade et al., 2010a; Feng et al. 2010; Senn et al., 2010; Sherman et al., 2010).

A lot of work still remains, specifically on the fractionation factors that govern isotope fractionation during chemical reactions affecting Hg speciation and reactivity. At the present state of the art, about fifteen laboratory experimental studies have been conducted on relevant reactions and have shown mercury isotopes fractionation in the environment. Because of its key role in the biogeochemical cycle, the Hg(II) reduction reaction in Hg^0 has mostly been studied. Hg(II) reduction occurs in a wide range of environmental reservoirs such as soils, water or sediments. The reaction occurs in light or dark environments, under oxic or anoxic conditions and can be promoted by biotic or abiotic agents (Gabriel and Williamson, 2004; Fitzgerald et al., 2007). Photoreduction of Hg(II) in water in the presence of dissolved organic matter (Bergquist and Blum, 2007; Zheng and Hintelmann, 2009) involves relatively small magnitude of mass dependent fractionation factors between the Hg(II) in solution and the Hg^0 produced ($1.0006 \leq {}^{202/198}\alpha_{Hg(II)/Hg^\circ} \leq 1.0012$). In dark conditions, the fractionation factor has been found to increase significantly ($1.0013 \leq {}^{202/198}\alpha_{Hg(II)/Hg^\circ} \leq 1.0020$). Furthermore,

photoreduction of Hg(II) was characterized by MIF in both works and displayed a large range of fractionation factors on the odd isotopes depending on the conditions ($1.001 \leq {}^{\Delta 199Hg}\alpha_{Hg(II)/Hg^{\circ}} \leq 1.006$). Reduction of Hg(II) in water was also conducted by using chemical reagents. Yang and Sturgeon (2008) reported a ${}^{202/198}\alpha_{Hg(II)/Hg^{\circ}}$ of 1.0005 for $SnCl_2$ and $NaBH_4$ reduction, with no significant MIF. Zheng and Hintelmann, (2010) found a ${}^{202/198}\alpha_{Hg(II)/Hg^{\circ}}$ of ~ 1.0016 for $SnCl_2$ reduction, here with significant MIF. Hg(II) reduction by four different bacterial strains promotes mass dependent processes with a limited range of fractionation factor ($1.0010 \leq {}^{202/198}\alpha_{Hg(II)/Hg^{\circ}} \leq 1.0021$, Kritee et al., 2007, 2008). Since many reducing agents and conditions lead to Hg(II) reduction in the environment, experimental works remain necessary to document fractionation factors related to other specific reactions.

This work reports the mercury isotope fractionation during Hg(II) abiotic reduction by a mixed Fe^{II}-Fe^{III} hydroxysalt green rust (GR). The GR is constituted of Fe^{II}-Fe^{III} hydroxide sheets separated by interlayer of anions and water molecules balancing the cation layer charge. GR is unstable under oxic conditions and thus found in transitional oxic and anoxic environments like hydromorphic soils (Trolard et al., 1997 ; Génin et al., 1998), ground water (Christiansen et al., 2009) or corroded iron based materials in marine environments or drinking water pipes (Refait et al., 2006). The name "fougerite" (IMA 2003-057) was attributed to this mineral (Trolard, 2006). The GR is considered as major actor in biogeochemical cycle (Herbillon, 2006; Borch et al., 2010), particularly for research on polluted soil and water remediation processes because of its high reactivity towards oxidized organic (nitroaromatics, chloride derived,…) or metallic compounds (Hg^{II}, Se^{VI}, Cr^{VI},…) (Myneni et al., 1997; Erbs et al., 1999; Loyaux-Lawniczak et al., 2000; Refait et al., 2000; O'Loughlin et al., 2003; Elsner et al., 2004).

Materials and Methods

Hydroxysulfate Green Rust Synthesis and Characterisation. The hydroxysulfate green rust 2 ($Fe^{II}_4Fe^{III}_2(OH)_{12}SO_4 \bullet 8H_2O$) (GR2) was synthesized by coprecipitation according to Gehin et al. (2002). Briefly, a mixture of ferrous sulphate heptahydrate $FeSO_4 \bullet 7H_2O$ and dehydrated ferric sulphate $Fe_2(SO_4)_3$ were dissolved in 100 mL of purified water (MilliQ+/MilliRO, Millipore, Billerica, MA) in a 200 mL flask with a $[Fe^{II}]/[Fe^{III}]$ ratio of 3 and $[Fe^{II}]+[Fe^{III}]$ = 0.2 M and 100 mL of NaOH 0.3 M were then added to the solution under magnetic stirring. After few seconds, the flask was sheltered from the air to avoid any oxidation. The GR2 was recovered by centrifugation (10 min 5,000 × *g*) and subsequently washed three times with filtered-sterilized and oxygen-free purified water (the water was previously boiled and cooled by bubbling with high purity N_2 through butyl rubber stopper). For the last wash, the GR2 was resuspended in a saline solution (3 mmol L^{-1} $FeSO_4 \bullet 7H_2O$) to get 31.2 $g.L^{-1}$ (i.e. 4 10^{-2} $mol.L^{-1}$) in final concentration for S1 – S5 experiments or in water for S0 and S6 experiments. The pH of the suspension was 6.9 ± 0.1. Aliquot of this suspension was dispatched in several flasks in order to get GR2 concentrations in the range 0.01 $mmol.L^{-1}$ to 3.27 mmol L^{-1} (Table 1). To prevent any dissolution of GR2 in water, dilutions were done in a solution of $FeSO_4 \bullet 7H_2O$ at 3 $mmol.L^{-1}$ for experiments S2, S3, S4 and S5 and 0.8 $mmol.L^{-1}$ for experiments B1 - B4. A solution of 3 $mmol.L^{-1}$ $FeSO_4 \bullet 7H_2O$ was done and used as a GR2-free control (experiments S0, Table 1). The concentration of GR2 ($Fe^{II}_4Fe^{III}_2(OH)_{12}SO_4 \bullet 8H_2O$) was estimated from the measurement of Fe^{II} and Fe^{tot} (Fe^{II} and Fe^{III} from the solid and aqueous phase) and by subtracting the contribution of $FeSO_4$ to Fe^{II} measurements.

The Fe^{II} and Fe^{tot} were measured according to Fadrus and Maly (1975) and by standard methods (APHA et al., 2004). Fe^{tot} was extracted by 6 $mol.L^{-1}$ HCl (final concentration). Aqueous Fe^{II} was measured on the filtered sample (0.2 μm porosity, Millex-GP SLGP,

Milipore, Billerica, MA) before acid extraction and under anaerobic atmosphere (Anoxic chamber, COY Laboratory Product. Inc., Grass Lake, MI).

The solids were characterized by X-ray diffraction (XRD) and transmission electronic microscopy (TEM). Briefly, the suspension was filtered under N_2 atmosphere, then the wet paste was spread out on a glass plate and coated with glycerol to prevent oxidation. The XRD data were collected with a D8 Bruker diffractometer, equipped with a monochromator and position-sensitive detector. The X-ray source was a Co anode (λ = 0.17902 nm). The diffractograms were recorded in the 3-64 2θ range, with a 0.0359° step size and a collecting time of 3 sec per point (Fig. 1a). For TEM observation, one drop of the suspension was laid on an amorphous carbon-coated grid and the sample was loaded into the microscope (Philips CM20/STEM).

The GR2 observed by TEM displayed crystal length from 0,2 μm up to 4 μm and exhibits a typical hexagonal geometry (Fig. 1b). The composition of these crystals (70%, 5% and 25% of O, S and Fe respectively) is characteristic of sulfated GR2 (Fig. 1c), electron diffraction (not shown) and XRD indicate d_{hkl} parameters specific of the GR2 (Fig. 1a).

Mercury Reduction by Green Rust: Experimental Setup. At initial time, Hg was introduced into the 100 mL glass reactor as Hg(II) using the standard reference material NIST 3133 at 9.95 ± 0.02 $mg.g^{-1}$ in 10% HNO_3 (v/v). A 0.1 mL aliquot of the Hg solution was added to the 50 mL of GR2 solution to reach ~ 19.9 $ng.mL^{-1}$ Hg into the reactor as initial concentration for each set of experiment. Mercury was added to various GR2 concentrations ranging from 0.01 to 3.27 $mmol.L^{-1}$ to spread the mercury-reduced fraction percentage (see Table 1 and discussion below). In order to monitor the evolution of the reaction and related isotopic variations, Hg(II) fractions were collected along with the time of the reaction (from 120 to 1800 seconds for experiments S0 to S6 or 120 to 3600 seconds for experiments B1 to B4). One mL of solution was withdrawn with a 1 mL disposable syringe, then filtered through

a 0.45 μm size pore filter and injected directly into 1 mL concentrated HNO_3 (69%, w/v, PROLABO®) in order to oxidize GR2 and thus stop the Hg(II) reduction reaction. Syringe and filter were further rinsed twice with 1mL purified water (18 MΩ). Six mL of purified water were finally added to the sub-sample to reach 10 % (v/v) HNO_3 concentration prior to Hg concentrations and isotopic analyses.

The reduction reaction of Hg(II) with GR2 leads to the formation of gaseous Hg^0 in the liquid. In order to outgas Hg^0, two methods were used. The first one (experiments S0 to S6) consisted in a mechanical agitation of the solution using a shaking apparatus. During all the reaction the reactor was continuously shaken and Hg^0 was removed from the liquid but not evacuated from the reactor. The second method (experiments B1 to B4) is based on a Hg free gas bubbling into the reactor to removed dissolved gases from water. Argon gas was introduced into the reactor via a syringe needle dipped into the solution. Ar bubble size was controlled and adjusted using a flow meter, and a second syringe needle was introduced through the septum to evacuate Ar (and Hg) gas avoiding any contact with ambient air.

Mercury Concentrations and Isotopic Analyses. Mercury concentrations in the GR2 solution aliquots were determined using cold vapour atomic absorption spectrometry (CV-AAS) at CRPG. Blank procedures were performed on GR2 aliquot (without Hg(II) added) using the same sampling procedure as describe above, including bubbling argon in purified water during 1 hour before sampling procedure. None of these two blank procedures revealed any Hg contamination (below the detection limit: 0.5 $ng.ml^{-1}$). Isotopic compositions of the Hg(II) fractions were measured using stannous chloride cold vapour generation coupled to a Neptune MC-ICP-MS (Thermo Scientific) at the Laboratoire des Mécanismes et Transfert en Géologie (LMTG, Toulouse, France) as described in Estrade et al., (2010b). Hg(II) was introduced in solution using the sample-standard bracketing technique and the isotopic

composition was reported as $\delta^{202}Hg(‰) = (\frac{^{202/198}Hg_{sample}}{^{202/198}Hg_{NIST3133}} - 1) \times 1000$ (Blum and Bergquist, 2007).

Samples and reference material were adjusted at 5 ng mL^{-1} into a 10% (v/v) HNO_3 matrix solution. At the time of the study (2006-2007), the reference material UM-Almaden was not available and the reference material CRPG-RL24H presented in Estrade et al. (2010b) was used. The external reproducibility of the method was ± 0.24 ‰ (2SD, n= 14) on the $\delta^{202}Hg$. In order to asses any effect due to the iron rich matrix during cold vapour generation or into the plasma, 1 mL of a concentrated GR2 sample (3.16 mmol.L^{-1}) was filtered and oxidized as described above and spiked with the NIST 3133 to reach 50 ng.mL^{-1} into 10 mL. This solution was then analysed against the NIST 3133 in 10% HNO_3 (v/v) matrix. Results do not show any deviation of the isotopic composition and are presented in Estrade et al. (2010b).

169 **Results and discussion**

170 **Reduction of Hg(II) to Hg^0 by Green Rust.** The reduction of Hg(II) by GR2 was
171 investigated by reacting 100 nmol.L^{-1} of Hg(II) with 0.01 mmol.L^{-1} to 1.3 mmol.L^{-1} of GR2 in
172 a continuously shaking mode (exp S0 to S6) and then with 0.88 mmol.L^{-1} to 3.27 mmol.L^{-1}
173 GR2 in a continuously bubbling mode (exp B1 to B4). Data on degassing methods, pH, Fe
174 and GR2 concentrations are summarized in Table 1 and Hg(II) concentrations are reported in
175 Table SI-S1.

176 Hg(II) was first injected into a solution of $FeSO_4 \bullet 7H_2O$ at 3 mmol.L^{-1} (exp S0, no GR2).
177 After 120 seconds, ~ 90% (f_{Hg}=0.89) of the initial mercury remained in solution and no further
178 evolution of the Hg(II) with the time was observed (Figure SI-S1a). Then, Hg(II) was injected
179 into a 0.01 mmol.L^{-1} GR2 solution in water containing only 0.04 mmol.L^{-1} Fe(II) (exp S1:
180 $FeSO_4$ was not added in the aqueous phase). After 120 seconds, the fraction of Hg(II)
181 remaining in solution was ~ 80% (f_{Hg}=0.79) (Figure SI-S1a). With increasing the quantity of
182 GR2 in suspension to 0.05 and 0.06 mmol.L^{-1} (exp S2 and S3) containing 3 mmol.L^{-1} $FeSO_4$
183 in solution, the Hg(II) fraction remaining was also 80% (f_{Hg}=0.79 and 0.80 respectively) after
184 120 seconds (Figure SI-S1b). At 0.5 mmol.L^{-1} GR2, the Hg(II) fraction remaining after 120
185 seconds decreased down to 40% (f_{Hg}=0.38 and 0.41) for exp S4 and S5 respectively (Figure
186 SI-S1c). For a 1.3 mmol.L^{-1} GR2 (exp S6) solution, the Hg(II) fraction remaining after 120
187 seconds reached 0.3% (f_{Hg}=0.003) (Figure SI-S1e).

188 These results showed that GR2 is the reducing agent of Hg(II) and suggested that the
189 reduction by GR2 proceeded almost instantaneously after the introduction of Hg(II). The fast
190 rate of reduction observed in these experiments has previously been documented by
191 O'Loughlin et al. (2003). These authors reported a reduction of 98.7% of the initial Hg(II)
192 after injection of Hg(II) at 400 μmol.L^{-1} to 6.4 mmol.L^{-1} of GR2, after 30 min. Here, we report
193 the reduction of up to 100% of Hg(II) by similar range of GR2 concentrations within 2 min.

The following aliquots through time of the experiment, showed a much lower decrease of remaining Hg(II) than the one observed for the first 120 seconds (exp S2 - S5). The evolution of Hg(II) with time does not suggest a classical kinetic of reduction (Figure SI-S1b,c). Experiments S2 to S5 present a decreasing trend of Hg(II) concentrations with time which do not fit an exponential decay as observed for other Hg(II) reduction by abiotic materials (e.g. Wiatrowski et al., 2009). Furthermore, erratic increases in Hg(II) concentration are not compatible with a smooth and regular Hg(II) reduction by GR2. Considering the Fe(II) concentrations in solution after reduction (exp S2 to S6), and according to reaction [1], GR2 was partially oxidized (1 mmol.L^{-1} of Fe(II) oxidized, see Table 1) by HNO_3 introduced at 2mmol.L^{-1} at initial time along with Hg(II).

$$Fe^{II}_4Fe^{III}_2OH_{12}SO_4(s) + 1/4NO_3^- + 3/2\ OH^- = SO_4^{2-} + 1/4NH_4^+ + 2Fe_3O_4(s) + 6H_2O \qquad [1]$$

The pseudo-first order rate constant (k_{obs}) derived from nitrate reduction by GR2 was ~ 0.2 $\times 10^{-5}$ s^{-1} from Hansen *et al.* (1996) under a pH of 8.1. The pH of the solution, in the present study, decreases from 6.9 to ~ 3. It is thus expected that just after mercury injection, GR2 reduces Hg(II) in solution and undergoes oxidation by HNO_3 due to the acidic pH conditions and according to equation [1]. Oxidation of GR2 will certainly result in the formation of new solid phases. TEM measurements were performed on the concentrated GR2 sample S1 (1.3 mmol.L^{-1}) in which ~ 80% of the initial Hg(II) was reduced in less than 120 seconds. No GR2 was observed at the end of the experiment, but at least three crystalline phases were observed (Fig. SI-S2). The electron diffraction pattern yielded the same d_{hkl} as magnetite (Fe_3O_4) platelet (Fig. SI-S2a), goethite (α-FeOOH) needle shape phase (Fig. SI-S2b), and hematite (α-Fe_2O_3) granular phase (Fig. SI-S2c). All those iron oxi-hydroxides are possible oxidation products of GR2 (Hansen et al., 1996; Hansen, 2001). Amongst GR2 oxidation by-products observed, magnetite is a mixed-valence iron oxide that contains both Fe(II) and Fe(III) and that has recently been documented to reduced Hg(II) in Hg^0 (Wiatrowski et al., 2009). TEM

images also revealed the presence of elemental Hg droplets associated with the granular phase (Figure 2a). The environment of these droplets is rich in Hg, O, Fe and sulfur (Figure 2b) suggesting that this phase corresponds to Hg^0 liquid droplets. After few minutes of electron radiations, the droplet collapsed and disappeared. This strongly supports the hypothesis that liquid Hg^0 droplets were trapped by the granular phase of GR2. These observations suggest a non-total efficiency of the shaking method to remove Hg^0 from the solution, which may be trapped onto the granular phase. Subsequently, these Hg^0 droplets can be withdrawn from the solution during the sub-sampling of the Hg(II) and get oxidized by dilution in concentrated nitric acid (see materials and methods). The sub-sampling of Hg^0 droplets may readily explain the erratic Hg concentrations with time observed for many experiments.

In order to better removed Hg^0 produced by the reduction and trapped onto the solid phase, a second set of experiments was conducted using argon bubbling method to outgas Hg^0 from the solution (exp B1 to B4). The evolution of Hg(II) concentrations remaining in solution with time for exp B1 and B2 (0.88 and 1.08 $mmol.L^{-1}$ GR2) are presented in Figure SI-S2d. 120 seconds after injection, a strong decrease in concentrations (f_{Hg}= 0.50 and 0.59 respectively for exp B1 and B2) is observed as reported in the case of shaking experiments. For the next 1200 seconds, a slower decrease in concentration than the one observed for the first 120 seconds (f_{Hg} fall down to 0.35 and 0.43 respectively for exp B1 and B2) occurred, as reported for the shaking experiments. Experiments B1 and B2 display a smooth distribution of Hg(II) through time and the absence of erratic increase of Hg(II) concentrations is attributed to the outgassing bubbling method.

Experiments B3 and B4 (and 1.42 and 3.27 $mmol.L^{-1}$ GR2) present f_{Hg}= 0.008 and 0.006 respectively, 120 seconds after Hg(II) injection. Evolution of the concentrations through time shows no significant increasing or decreasing trend but rather display an erratic distribution suggesting, here again, the sampling of Hg^0 droplets adsorbed onto the solid phase although

Ar bubbling was used. The drastic decrease in concentration observed in exp B3 and B4 is attributable to the Hg(II) reduction by the GR2 as for exp S6.

For this second set of experiment, GR2 concentrations of 0.88 and 1.08 mmol.L^{-1}, (B1 and B2 respectively) reduced a lower amount of Hg(II) (~ 50%) than shaking experiments with 0.5 mmol.L^{-1} GR2 (exp S4 and S5: ~ 60% Hg(II) reduced). However, increasing GR2 concentrations to 1.4 and 3.2 mmol.L^{-1} (exp B3 and B4) resulted in only 0.6% of Hg(II) remaining in solution, only 120 seconds after injection (against 0.3% for exp S6 see above) which indicates also less reduction than shaking experiments for the same quantity of GR2 in solution. Nevertheless, the magnitudes of reduction for these two sets of experiments (bubbling versus shaking experiments) are similar. The use of two different preparations of initial GR2 and two different techniques to outgas Hg^0, likely explains the small difference in reduction efficiency.

To conclude this part, the reaction mechanism observed in these experiments did not allow to observe a direct and only reduction of the Hg(II) by the GR2. Subsequent and intermediate reactions were certainly involved: 1) the oxidation of GR2 resulted in by-products, themselves able to reduce Hg(II) remaining in solution (e.g. magnetite) (exp S2 - S6, B1 and B2); 2) the trapping of liquid Hg^0 droplets observed onto the solid phase in solution may have led to an overestimation of the Hg(II) remaining in solution (all experiments).

Mercury Isotope Fractionation During Green Rust Reduction. Only selected Hg(II) aliquot were analysed for their isotopic composition and are presented in Table SI-S2. Considering the whole dataset, Hg(II) fractions remaining in solution after the reduction yielded a range of isotopic ratios and displayed mass dependent fractionation as presented in a $\delta^{202}Hg$ versus $\delta^{201}Hg$ diagram (Fig. SI-S3). Isotopic compositions measured in these experiments may originate from several processes such as Hg(II) reduction by green rust and subsequent Hg(II) reduction as well as Hg^0 trapped onto the mineral phase. Nevertheless, it

appears that all these processes lead to mass dependent fractionation. In the following, isotopic composition of Hg(II) fractions remaining in solution will be described using $\delta^{202}Hg$ values relative to the starting material (NIST 3133). Except for samples from experiments S6, B3 and B4, for which the initial Hg(II) was almost entirely reduced and evacuated from the solution, all the measured $\delta^{202}Hg$ values are positive. This suggests that the reduction of Hg(II) by GR2 lead to Hg^0 depleted in heavy mercury, similar to reduction reactions induced by other reducing agents (Kritee et al., 2007; 2008; Yang and Sturgeon, 2008; Zheng and Hintelmann, 2010). Samples from experiments S6, B3 and B4 yielded a larger range of $\delta^{202}Hg$ values, both positive and negative. This is surprising because one would expect highly positive $\delta^{202}Hg$ values of residual Hg when >99% of the initial Hg(II) was reduced. Negative $\delta^{202}Hg$ values certainly characterize the reduction product Hg^0. It was shown above that not all Hg^0 was evacuated from the solution as we observed Hg^0 droplets adsorbed on solution particles (Fig. 2). These may have been sampled along with residual Hg(II) and readily explain the low and negative $\delta^{202}Hg$ values measured for experiment S6, B3 and B4 samples. These Hg^0 droplets may have formed all along the reduction experiment and integrated the composition of the reaction product over a certain time. A minimum $\delta^{202}Hg$ value measured would suggest a maximum of Hg^0 contribution to the sample. Therefore, a $\delta^{202}Hg$ value of -1.14‰ (Tab. SI-S2) would indicate a minimum fractionation between Hg(II) and Hg^0 during the reduction reaction of the B4 experiment. Samples from the other experiments (S2 to S5) were plotted in Rayleigh diagrams in order to see if the measured isotopic composition would fit a distillation effect with a fractionation factor α of ca. 1.00114 between Hg(II) and Hg^0 (Fig. SI-S4). For all the experiments, all the data do not align along the evolution curve corresponding to $\alpha = 1.00114$ but rather fall between curves corresponding to α of 1.0013 and 1.0005. According to the Rayleigh fractionation equation ($R/R_i = f^{\left(\frac{1}{\alpha}-1\right)}$), with R and R_i,

293 respectively the isotopic ratios during the reaction and at initial time (Hoefs, 1987), the
294 overall fractionation process is characterized by a constant fractionation factor between the
295 initial Hg(II) and the Hg^0 produced ($\alpha^{202}_{Hg(II)/Hg^\circ}$). Figure 3b presents $ln(R/R_i)$ versus $-lnf_{Hg}$,
296 where (R/R_i) is represented by $(1+\delta^{202}Hg/1000)$. In such a diagram, $\alpha^{202}_{Hg(II)/Hg^\circ}$ can be
297 extracted from the slope of the linear relationship. Calculation of the slope using Isoplot® X-Y
298 regression software led to a global $\alpha^{202}_{Hg(II)/Hg^\circ}$ of 1.000 94 ± 0.000 44 (2SD, n= 20 excluding
299 S6, B3 and B4 experiments). $\alpha^{202}_{Hg(II)/Hg^\circ}$ display a large uncertainty associated to a weak
300 determination coefficient (r^2=0.56 for the relationship $ln(R/R_i)$ vs $-lnf_{Hg}$). The fractionation
301 factor calculated from the slope in the diagram of Fig. 3b is certainly only "apparent" and do
302 not represent the real $\alpha^{202}_{Hg(II)/Hg^\circ}$ of the reduction reaction. All these observations suggest that
303 many samples may have contained small contributions of Hg^0 droplets so that the measured
304 isotopic composition yielded lower $\delta^{202}Hg$ values than that of residual Hg(II) of our
305 experiments.

306 **Environmental implications.** This work reports a very rapid Hg(II) reduction rate by GR2.
307 This confirms that GR2 can be an effective reducing agents for mercury in anoxic/suboxic
308 environments. Experimental settings used in this work consisted in introducing Hg(II) with
309 HNO_3 in order to be able to sample a large range of Hg(II) fractions remaining in solution.
310 The transformation of GR2 into oxidation products such as magnetite and others mineral
311 phases indicated that subsequent reactions may play a significant role in the fate of residual
312 Hg(II) and Hg^0 produced. Hg(II) can undergo subsequent reduction and Hg^0 produced may
313 adsorbed onto the minerals formed by the oxidation of GR2. Our experiments can thus be
314 compared to a simple, but nevertheless realistic, environmental medium where several
315 reactions such as reduction and adsorption may take place simultaneously or continuously.
316 The isotope fractionation processes observed during these reactions are all mass dependent.
317 The isotopic composition of Hg(II) fractions remaining in solution of most experiments

showed an enrichment in the heavier isotopes suggesting fractionation factor ($^{202/198}\alpha_{Hg(II)/Hg^0}$) of 1.0013. This value is considered minimum because we suspect that some Hg^0 with negative $\delta^{202}Hg$ may have been present in our samples. The fractionation factor determined here has an intermediate value compared to fractionation factors reported in the literature for reduction with organic matter, chemical or bacterial assemblages or photoreduction of Hg(II). For example, the maximum fractionation factor for reduction (bacterial reduction) was found to be around 1.002 for the $^{202/198}\alpha_{Hg(II)/Hg^0}$ (Kritee et al. 2007; 2008). Compared to other processes that show large fractionation factor (e.g. evaporation; Estrade et al., 2009), reduction will imply large Hg mass dependent isotope fractionation only if large amount of Hg is reduced within a given reservoir. In terrestrial environments, Hg(II) to Hg^0 reduction is a reaction that will increase the mobility of mercury (Borch et al., 2010; Gabriel and Williamson, 2004). However, estimations of the amount and the importance of Hg(II) reduction in environmental reservoirs such as sediments and soils, combined to the relatively small related fractionation factors, will not result in significant isotope fractionation of the $^{202/198}Hg$ ratio relative to the starting Hg stock. This suggests that Hg in soils may keep its original isotopic composition, opening the possibility of isotope source tracing of polluted areas.

Acknowledgments We would like to thank Jeroen Sonke and Remy Freydier for analytical assistance on the LMTG Neptune. Luc Marin and Jitka Lhomme (CRPG-SARM) for their technical support and Asfaw Zegeye for the GR2 synthesis. This is the CRPG contribution XXXX.

Supporting Information Available Additional data, tables, method descriptions and discussion are provided in supporting information. This material is available free of charge via the internet at http://pubs.acs.org.

342 **Litterature cited**

343 APHA, WWA and WEF. In *Standard Methods for the Examination of Water and Wastewater*,
344 20th ed.; Clersceri, L.S.; Greenberg, A. E.; Eatol, A. D. Eds.; Am. Public Health
345 Association, Am. Water Works Association, Water Environ. Fed.; Washington, DC,
346 1998.

347 Bergquist, B. A.; Blum, J. D., Mass-dependent and -independent fractionation of Hg isotopes
348 by photoreduction in aquatic systems. *Science* **2007,** *318*, (5849), 417-420.

349 Blum, J. D.; Bergquist, B. A., Reporting of variations in the natural isotopic composition of
350 mercury. *Anal. Bioanal. Chem.* **2007,** *388*, (2), 353-359.

351 Borch, T.; Kretzschmar, R.; Kappler, A.; Van Cappellen, P.; Ginder-Vogel, M.; Voegelin, A.;
352 Campbell, K., Biogeochemical Redox Processes and their Impact on Contaminant
353 Dynamics. *Environ. Sci. Tech.* **2010,** *44*, (1), 15-23.

354 Carignan, J.; Estrade, N.; Sonke, J. E.; Donard, O. F. X., Odd Isotope Deficits in Atmospheric
355 Hg Measured in Lichens. *Environ. Sci. Technol.* **2009,** *43*, (15), 5660-5664.

356 Christiansen, B. C.; Balic-Zuni, T.; Dideriksen, K.; Stipp, S. L. S. Identification of green rust
357 in groundwater. *Environ. Sci. Technol.* **2009**, *43,* 3436-3441.

358 Elsner, M.; Schwarzenbach, R.; Haderlein, S. B. Reactivity of iron(II) bearing minerals
359 towards reductive transformation of organic contaminants. *Environ. Sci. Technol.* **2004**,
360 *38***,** 799-807.

361 Erbs, M; Hansen, H. C. B.; Olsen, C.E. Reductive dechlorination of carbon tetrachloride
362 using iron(II) iron(III) hydroxide sulfate (green rust). *Environ Sci Technol* **1999**, *33*,
363 307-311.

364 Estrade, N.; Carignan, J.; Sonke, J. E.; Donard, O. F. X., Mercury isotope fractionation
365 during liquid-vapor evaporation experiments. *Geochim. Cosmochim. Acta* **2009,** *73*,
366 (10), 2693-2711.

367 Estrade, N.; Carignan, J.; Sonke, J. E.; Donard, O. F. X., Isotope tracing of atmospheric
368 mercury sources in an urban area of northeastern France. *Environ. Sci. Technol.* **2010,**
369 in press.
370 Estrade, N.; Carignan, J.; Sonke, J. E.; Donard, O. F. X., Measuring Hg isotopes in bio-geo-
371 environmental reference materials. *Geostand. Geoanal. Res.* **2010,** *34*, (1), 79-93.
372 Fadrus, H.; Maly, J. Suppression of iron(III) interference in the determination of iron(II) in
373 water by the 1,10-phenanthroline method. *Analyst*, **1975***, 100*, 549-554.
374 Feng, X. B.; Foucher, D.; Hintelmann, H.; Yan, H. Y.; He, T. R.; Qiu, G. L., Tracing Mercury
375 Contamination Sources in Sediments Using Mercury Isotope Compositions. *Environ.*
376 *Sci. Technol.* **2010,** *44*, (9), 3363-3368.
377 Fitzgerald, W. F.; Lamborg, C. H.; Hammerschmidt, C. R., Marine biogeochemical cycling
378 of mercury. *Chem. Rev.* **2007,** *107*, (2), 641-662.
379 Foucher, D.; Ogrinc, N.; Hintelmann, H., Tracing Mercury Contamination from the Idrija
380 Mining Region (Slovenia) to the Gulf of Trieste Using Hg Isotope Ratio Measurements.
381 *Environ. Sci. Technol.* **2009,** *43*, (1), 33-39.
382 Gabriel, M. C.; Williamson, D. G., Principal biogeochemical factors affecting the speciation
383 and transport of mercury through the terrestrial environment. *Environ. Geochem. Health*
384 **2004,** *26*, (4), 421-434.
385 Génin, J.-M. R.; Bourrié, G.; Trolard, F.; Abdelmoula, M.; Jaffrezic, A.; Refait, P.; Maître,
386 V.; Humbert, B.; Herbillon, A. Thermodynamic equilibria in aqueous suspensions of
387 synthetic and natural Fe(II) - Fe(III) green rusts; occurences of the mineral in
388 hydromorphic soils. *Environ. Sci. Technol.* **1998**, *32***,** 1058-1068.
389 Géhin, A.; Ruby, C.; Abdelmoula, M.; Benali, O.; Ghanbaja, J.; Refait, P.; Génin, J.-M. R.
390 Synthesis of Fe(II-III) hydroxysulphate green rust by coprecipitation. *Solid State Sci.*,
391 **2002**, *4*, 61-66.

392 Gustin, M.; Jaffe, D., Reducing the Uncertainty in Measurement and Understanding of
393 Mercury in the Atmosphere. *Environ. Sci. Tech.* **2010,** *44*, (7), 2222-2227.
394 Hansen, H. C. B.; Koch, C. B.; Nancke-Krogh H.; Borggaard, O. K; Sørensen, J. Abiotic
395 nitrate reduction to ammonium: key role of green rust. *Environ. Sci. Tech.* **1996**, *30*,
396 2053-2056.
397 Hansen, H. C. B. Environmental chemistry of iron(II)-iron(III) LDHs. In : *Layered Double*
398 *Hydroxides: Present and Future;* Boriotti, S. and Dennis, D. Eds.; Nova Science
399 Publishers Inc., Huntington, NY, 2001; pp. 413-34.
400 Herbillon, A. J. Ferrosic hydroxides, green rusts and fougerite in the biogeochemical cycle of
401 iron. *C.R. Geosciences* **2006**, *338*, 393-401.
402 Hoefs J. *Stable Isotope Geochemistry (third ed.)*; Springer-Verlag, Berlin, 1987.
403 Kritee, K.; Blum, J. D.; Johnson, M. W.; Bergquist, B. A.; Barkay, T., Mercury stable isotope
404 fractionation during reduction of Hg(II) to Hg(0) by mercury resistant microorganisms.
405 *Environ. Sci. Technol.* **2007,** *41*, (6), 1889-1895.
406 Kritee, K.; Blum, J. D.; Barkay, T., Mercury Stable Isotope Fractionation during Reduction of
407 Hg(II) by Different Microbial Pathways. *Environ. Sci. Technol.* **2008,** *42*, (24), 9171-
408 9177.
409 Lindberg, S.; Bullock, R.; Ebinghaus, R.; Engstrom, D.; Feng, X. B.; Fitzgerald, W.; Pirrone,
410 N.; Prestbo, E.; Seigneur, C., A synthesis of progress and uncertainties in attributing the
411 sources of mercury in deposition. *Ambio.* **2007,** *36*, (1), 19-32.
412 Loyaux-Lawniczak, S.; Refait, P.; Ehrhardt, J.-J.; Lecomte, P.; Génin, J.-M. R. Trapping of
413 Cr by formation of ferrihydrite during the reduction of chromate ions by Iron (II)-
414 Iron(III) hydroxysalt green rusts. *Environ Sci. Technol.* **2000**, *34*, 438-443.
415 Myneni, S. C. B.; Tokunaga, T. K.; Brown Jr., G.E. Abiotic Se redox chemistry in the
416 presence of Fe(II, III)-oxides. *Science*, **1997**, *278*, 1106-1109.

O'Loughlin, E. J.; Kelly, S. D.; Kemner, K. M.; Csencsits, R.; Cook, R. E. Reduction of Ag^{I}, Au^{III}, Cu^{II}, and Hg^{II} by Fe^{II}/Fe^{III} hydroxysulfate green rust. *Chemosphere* **2003**, *53*, 437-446.

Refait, P.; Abdelmoula, M.; Génin J.-M. R.; Sabot, R. Green rusts in electrochemical and microbially influenced corrosion of steel. *C.R. Geosciences* **2006**, *338*, 476-487.

Refait, P.; Simon, L.; Génin J.-M. R. Reduction of SeO_4^{2-} anions and anoxic formation of iron(II)-iron(III) hydroxy selenate green rust. *Environ. Sci. Technol.* **2000***, 34*, 819-825.

Selin, N. E., Global Biogeochemical Cycling of Mercury: A Review. *Annu. Rev. Env Resour.* **2009,** *34*, 43-63. Senn et al., 2010;

Sherman et al., 2010;

Trolard, F. Fougerite: from field experiment to the homologation of the mineral. *C. R. Geoscience* **2006**, *338*, 1158-1166.

Trolard, F.; Génin, J.-M. R.; Abdelmoula, M.; Bourrié, G.; Humbert, B.; Herbillon, A. Identification of a green rust mineral in a reductomorphic soil by Mössbauer and Raman spectroscopies. *Geochim. Cosmochim. Acta* **1997**, *61*, 1107-1111.

Wiatrowski, H. A.; Das, S.; Kukkadapu, R.; Ilton, E. S.; Barkay, T.; Yee, N., Reduction of Hg(II) to Hg(O) by Magnetite. *Environ. Sci. Tech.* **2009,** *43*, (14), 5307-5313.

Yang, L.; Sturgeon, R., Isotopic fractionation of mercury induced by reduction and ethylation. *Anal. Bioanal. Chem.* **2009,** *393*, (1), 377-385.

Zheng, W.; Hintelmann, H., Mercury isotope fractionation during photoreduction in natural water is controlled by its Hg/DOC ratio. *Geochim. Cosmochim. Acta* **2009,** *73*, (22), 6704-6715.

Zheng, W.; Hintelmann, H., Nuclear field shift effect in isotope fractionation of mercury during abiotic reduction in the absence of light. *J. Phys. Chem. A* **2010,** *114*, (12), 4238-4245.

442 **Figure captions**

443

444 Figure 1. X-ray diffraction of the sulphated green rust 2 chemically synthesized (a). TEM
445 image (b) and composition (c, as determined by EDX) of the hexagonal crystals. GR2 denotes
446 d_{hkl} (in Å) of the green rust 2.

447 Figure 2: TEM image of solids after oxidation phase with Hg/HNO_3 showing a Hg^0 droplet
448 into a hematite–like phase (a), and composition of the droplet as determined by EDX (b). The
449 inset image corresponds to the electron diffraction of the hematite-like phase.

450 Figure 3: a) Isotopic compositions of the Hg(II) fractions remaining in solution ($\delta^{202}Hg$) for
451 the whole dataset plotted against the Hg(II) fractions remaining in solution (f_{Hg}). The
452 progressive enrichment in the heavier isotopes for the Hg(II) fractions remaining in solution
453 ($f_{Hg} \rightarrow 0$ excepted) indicates Rayleigh distillation process during the reduction of the Hg(II). b)
454 $ln(1+\delta^{202}Hg/1000)$ plotted against $-lnf_{Hg}$,. The fractionation factor between the Hg(II) and the
455 Hg^0 produced extracted from the slope yield a value of 1.00094 ± 0.00044 (2SD) associated
456 with a weak determination coefficient (r^2=0.56). These uncertainties reflect an apparent
457 fractionation factor due to subsequent processes. In figure a) fractions with negative $\delta^{202}Hg$
458 suggest the sampling of Hg^0 droplets (reduction product), implying a minimum fractionation
459 between the Hg(II) and the Hg^0 of 1.14 ± 0.24 ‰ ($\Delta^{202}Hg_{Hg(II)-Hg^0}$) (see text).

460

Tables

Table 1: Summary of pH and Fe and GR2 concentrations for each experiment before and after oxidation.

	Before oxidation						After oxidation	
Exp N°	**pH**	**Fe_{tot}[a] (mM)**	**Fe_{GR2}[b] (mM)**	**GR2 (mM)**	**GR2 (g L^{-1})**	**Total Fe^{IIc} (mM)**	**pH**	**Total Fe^{IIc} (mM)**
	Continuous shaking mode							
S0	6.9	3.01	*0.00*	*0.00*	*0.00*	2.95	n.d.	2.99
S1	6.9	0.06	*0.06*	*0.01*	*0.01*	*0.04*	n.d.	n.d.
S2	6.9	3.34	*0.34*	*0.06*	*0.04*	2.67	n.d.	2.72
S3	6.9	3.33	*0.32*	*0.05*	*0.04*	3.28	n.d.	2.82
S4	6.9	6.03	*3.02*	*0.50*	*0.39*	5.09	n.d.	3.92
S5	6.9	5.98	*2.97*	*0.50*	*0.39*	4.97	n.d.	4.27
S6	6.9	7.82	*7.82*	*1.30*	*1.01*	*5.21*	n.d.	n.d.
	Continuous bubbling mode							
B1	6.8	6.10	*5.30*	*0.88*	*0.69*	4.1	3.1	n.d.
B2	6.8	7.30	*6.50*	*1.08*	*0.84*	4.7	3.0	n.d.
B3	6.8	8.90	*8.50*	*1.42*	*1.10*	5.65	2.8	n.d.
B4	6.8	20.40	*19.60*	*3.27*	*2.55*	11.5	3.5	n.d.

The italic values correspond to an estimation made from the measures. S0 & B0 = control ($FeSO_4$ solution). n.d. = not determined.

[a] $Fe_{tot} = Fe^{II} + Fe^{III}$ (aqueous and solid) excepted for S1 & S6 where no $FeSO_4$ was added.

[b] $Fe_{GR2} = Fe_{tot} - Fe_{control}$

[c] Total $Fe^{II} = Fe^{II}_{aq} + Fe^{II}_{s}$

469 **Figures**

470 Figure 1

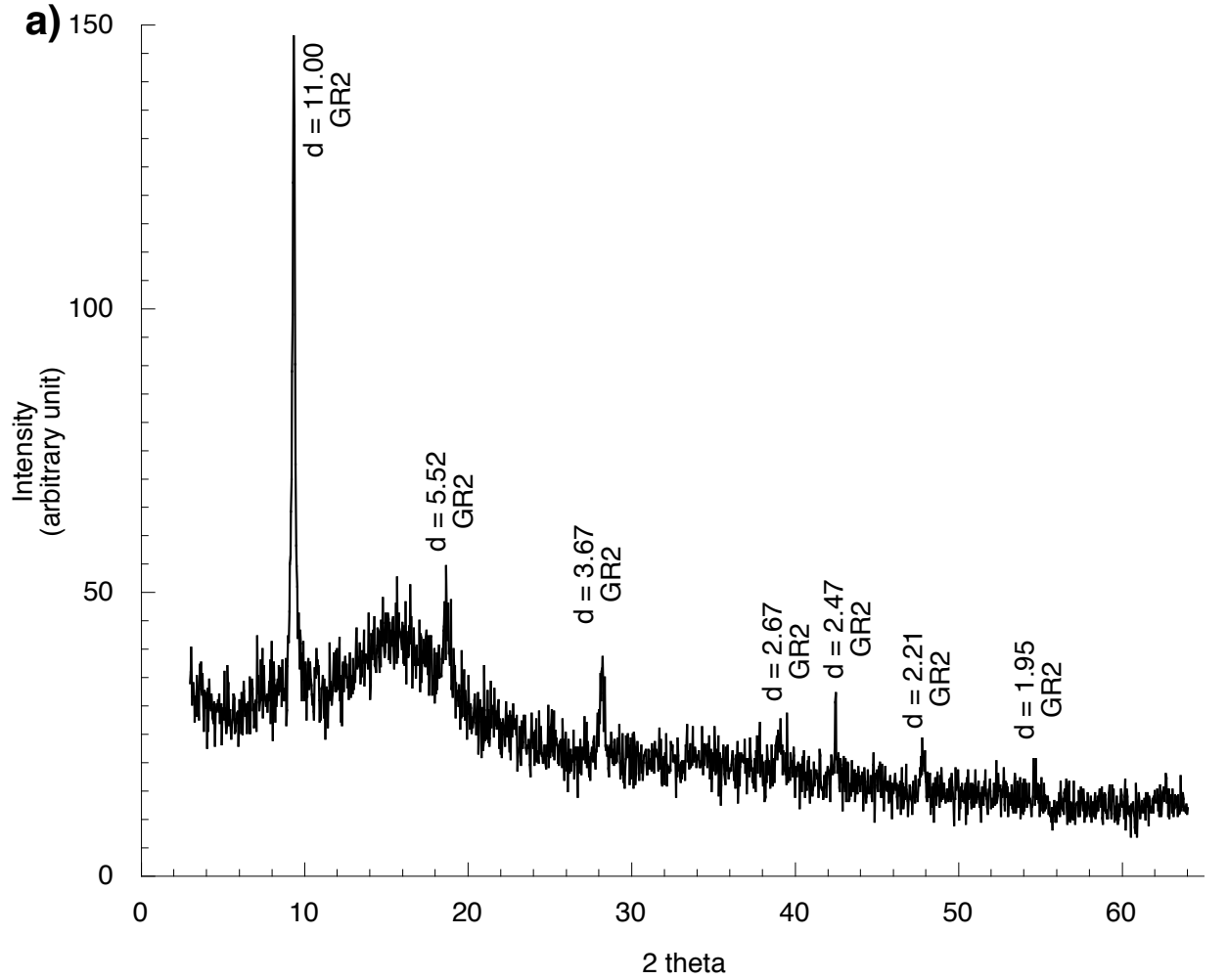

471

472

473

474

475

476

477

478

479 Figure 2

480

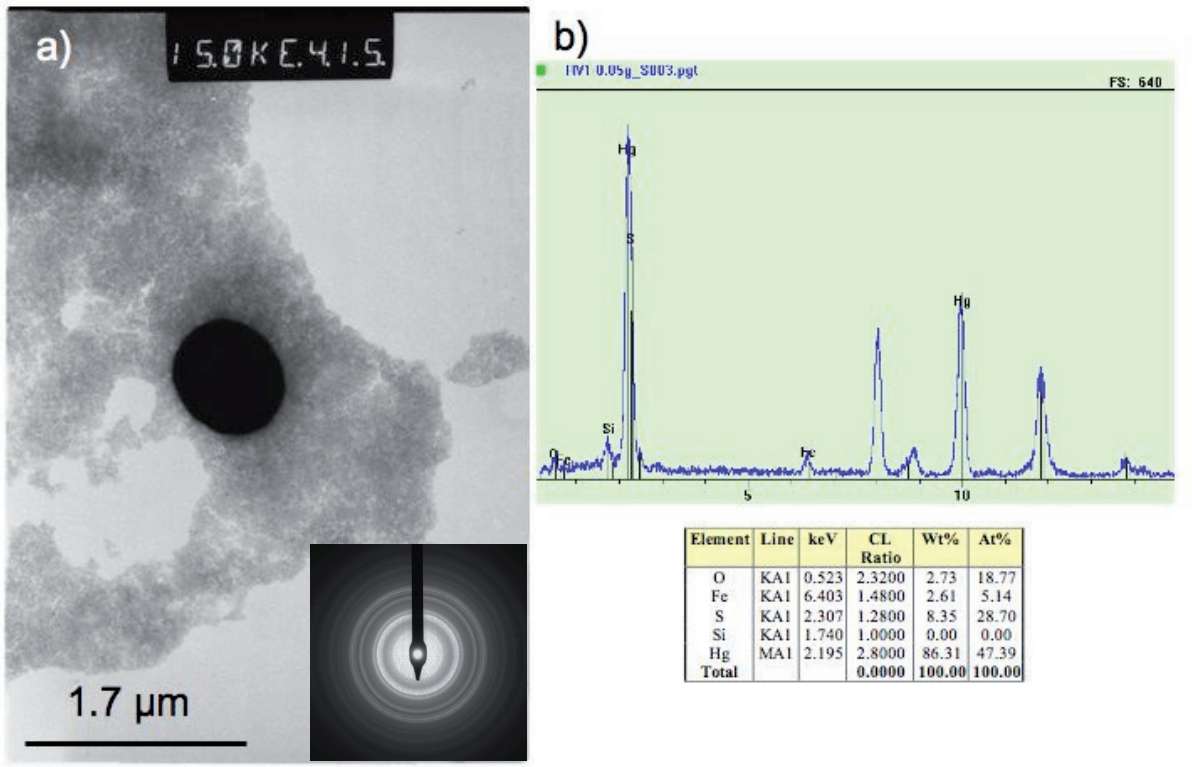

Element	Line	keV	CL Ratio	Wt%	At%
O	KA1	0.523	2.3200	2.73	18.77
Fe	KA1	6.403	1.4800	2.61	5.14
S	KA1	2.307	1.2800	8.35	28.70
Si	KA1	1.740	1.0000	0.00	0.00
Hg	MA1	2.195	2.8000	86.31	47.39
Total			**0.0000**	**100.00**	**100.00**

481 Figure 3

482

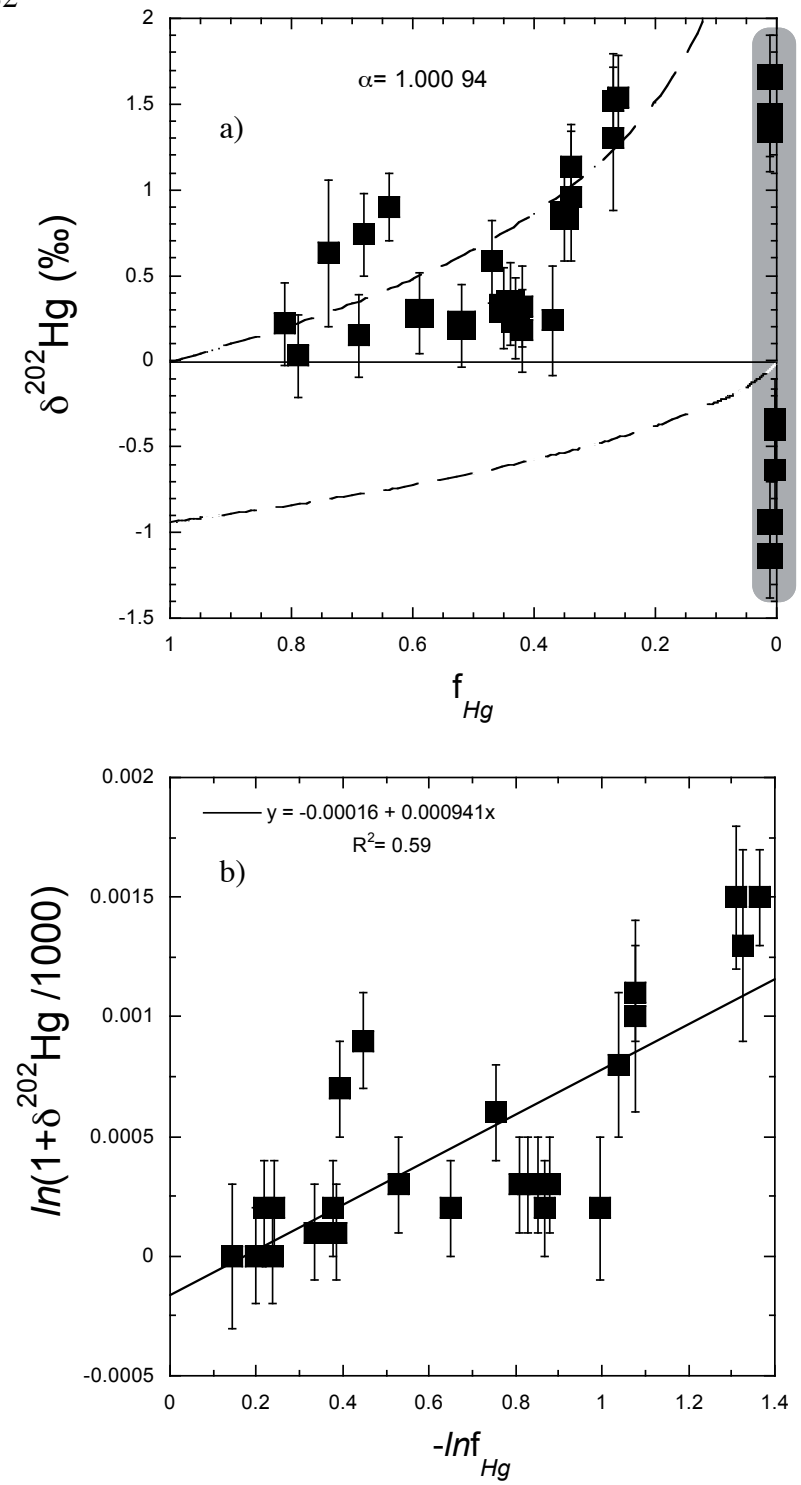

Supporting Information

Mercury isotope fractionation during abiotic reduction by the hydroxysulfate green rust 2

Nicolas Estrade, Jean Carignan, Frédéric Jorand and Olivier F.X. Donard

8 pages (including title page)

4 Figures (SI-S1 to SI-S4)

2 Tables (SI-S1 and SI-S2)

Figure SI-S1: Hg(II) concentration remaining in solution in function of the time, a) S0: FeSO4 solution GR2= 0.00 mM, S1: GR2= 0.01 mM mechanical agitation , b) S2: GR2= 0.06 mM, S3: GR2= 0.05 mM mechanical agitation c) S4 and S5: GR2= 0.5 mM, mechanical agitation d)) B3: GR2= 1.08 mM, B4: GR2= 0.88 mM bubbling e) S6: GR2= 1.3 mM mechanical agitation, B2: GR2= 1.42 mM and B3: GR2= 3.27 mM bubbling

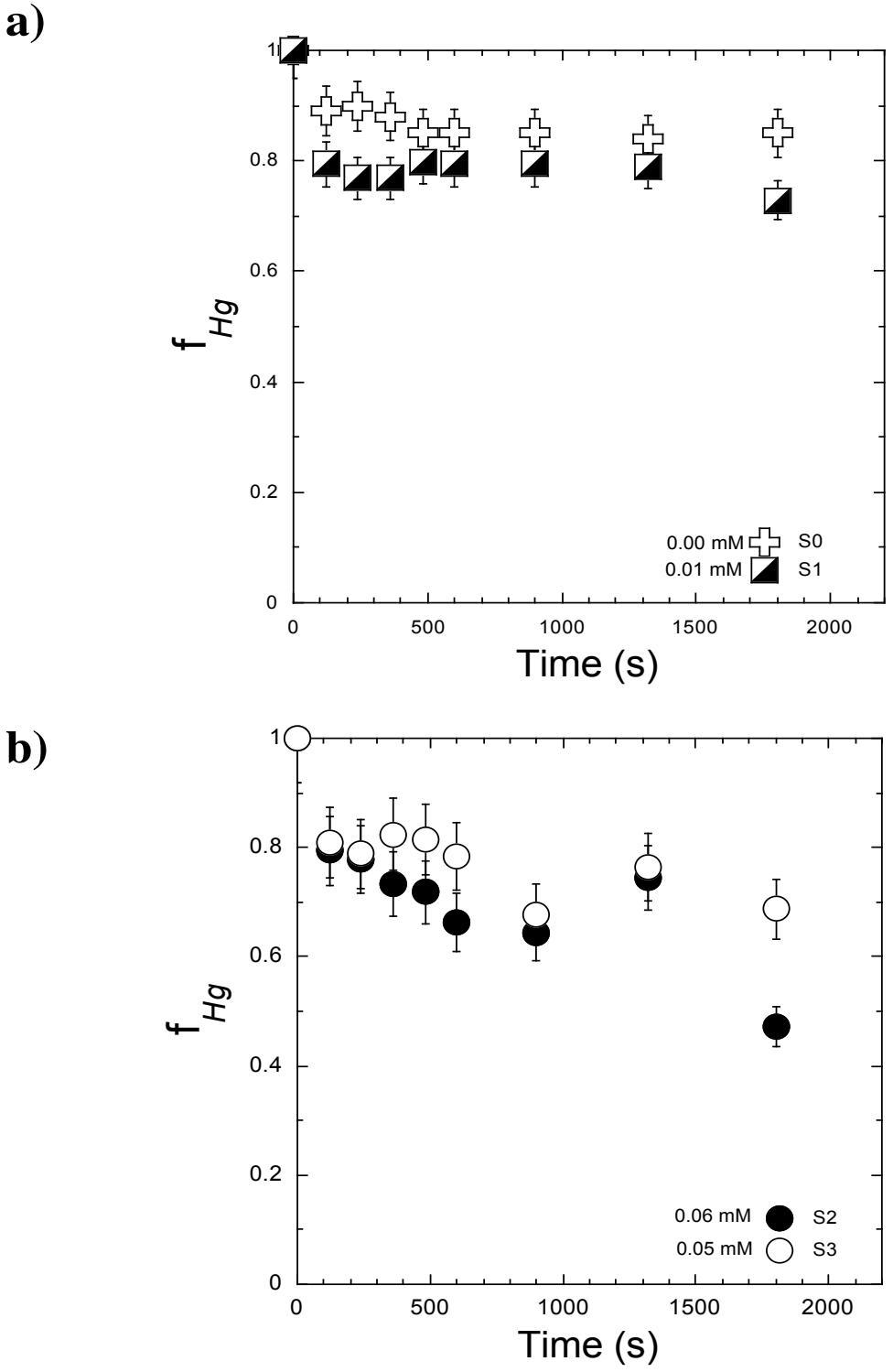

S2

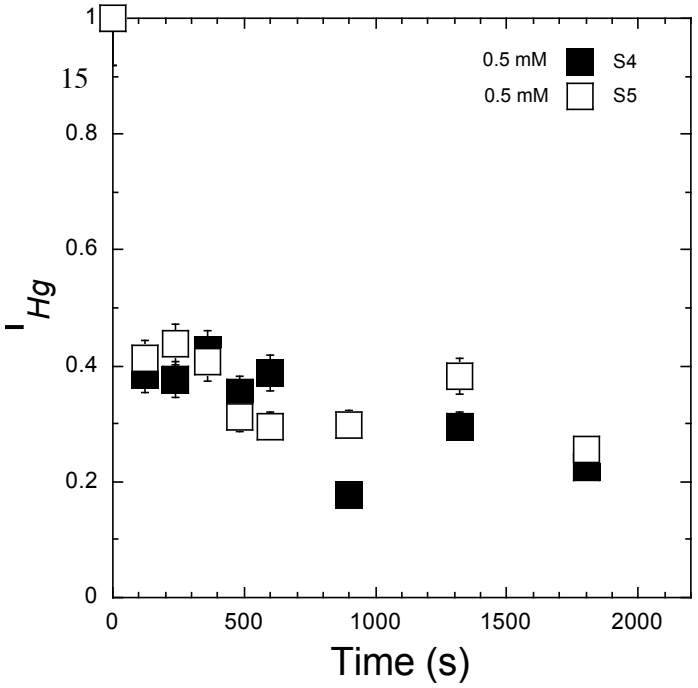
0.5 mM S4
0.5 mM S5
$\Delta^{199}Hg$
Time (s)

c)

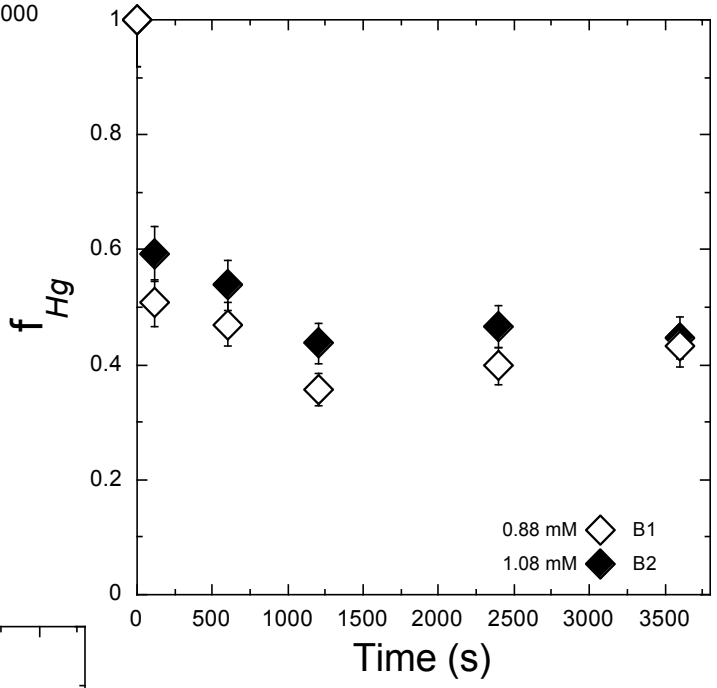
0.88 mM B1
1.08 mM B2
f_{Hg}
Time (s)

d)

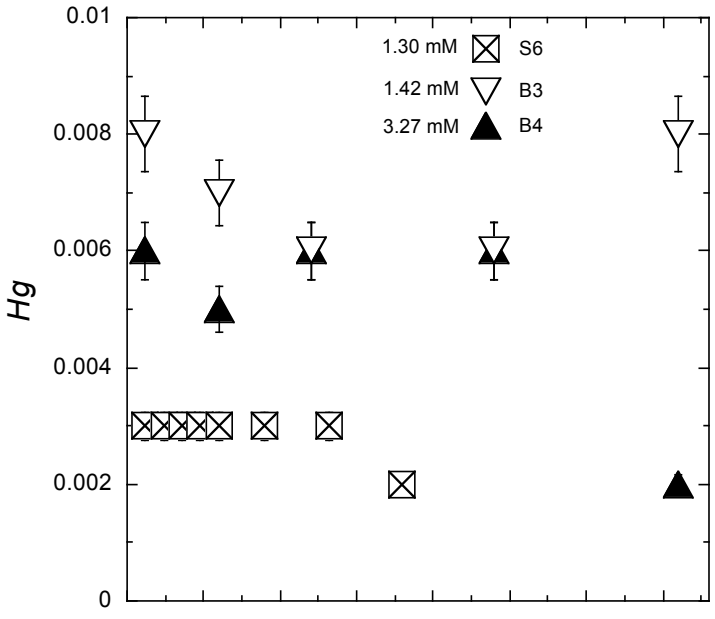
1.30 mM S6
1.42 mM B3
3.27 mM B4
$\Delta^{200}Hg$

e)

S3

Figure SI-S2: TEM images of solid phases after oxidation in presence of Hg/HNO_3 with the corresponding electron diffractogram. a) magnetite phase, b) goethite phase, c) hematite phase.

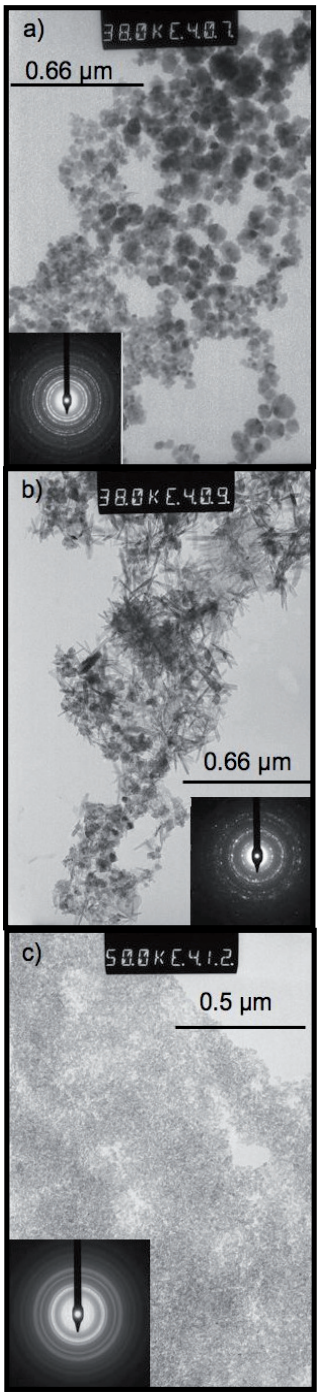

Figure SI-S3: Isotopic composition of all the Hg(II) fractions remaininig in solution plotted in a diagram $\delta^{201}Hg$ vs $\delta^{202}Hg$. In this diagram, no deviation of the theoritical relationship $\delta^{201}Hg$ (‰) vs $\delta^{202}Hg$ incates that the reduction mechanism depends upon on mass.

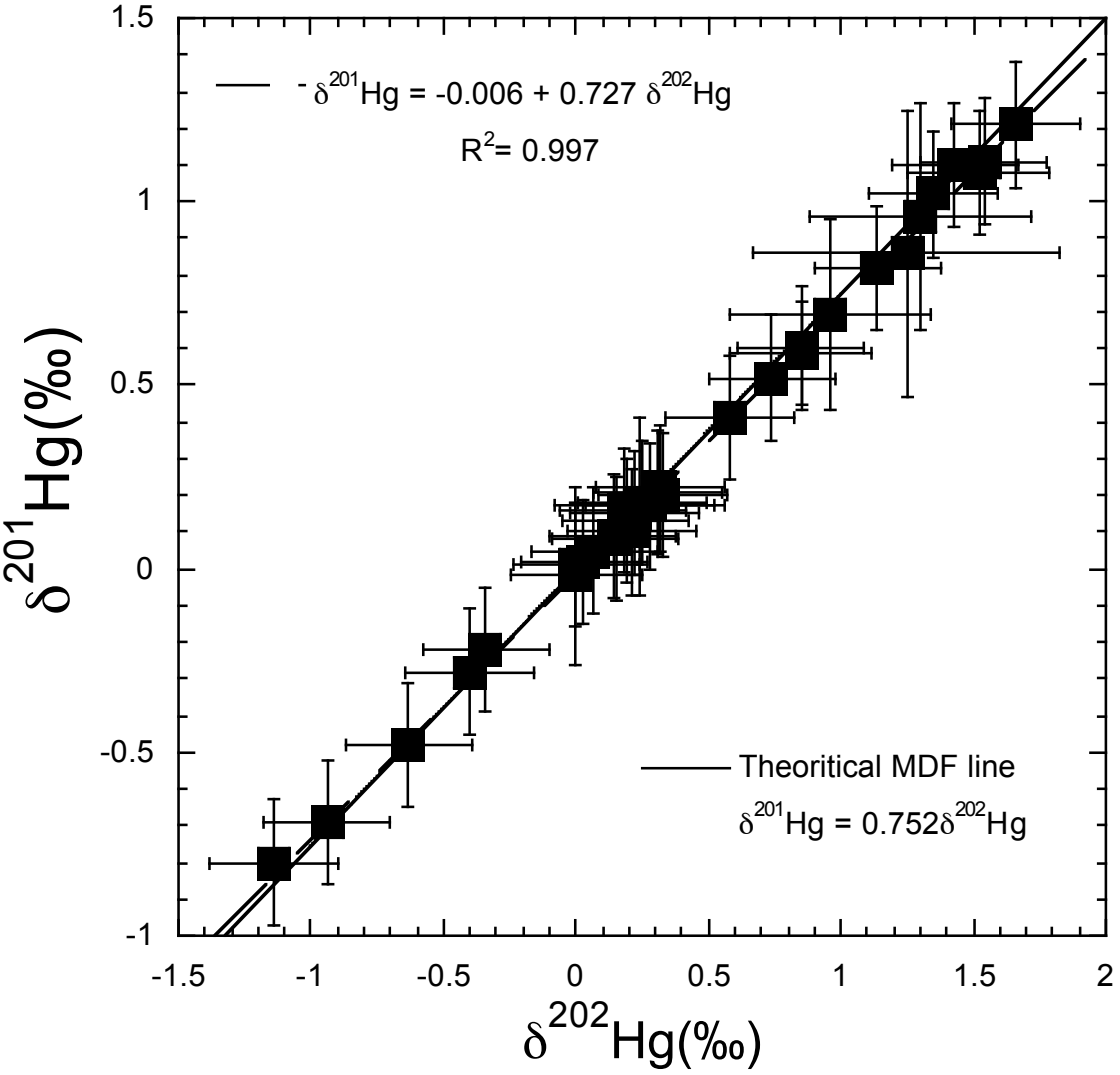

Figure SI-S4: Rayleigh fractionation diagram where δ^{202}Hg of the Hg(II) remaining fractions is plotted against f_{Hg}. Data were individualyzed by GR2 concentrations range. Dashed lines represents Rayleigh fractionation modeling with a fractionationation factor comprise between 1.0005 and 1.00114. a) experiments S6, B3, B4; b) experiments S2, S3; c) experiments S4, S5; d) experiments B1, B2.

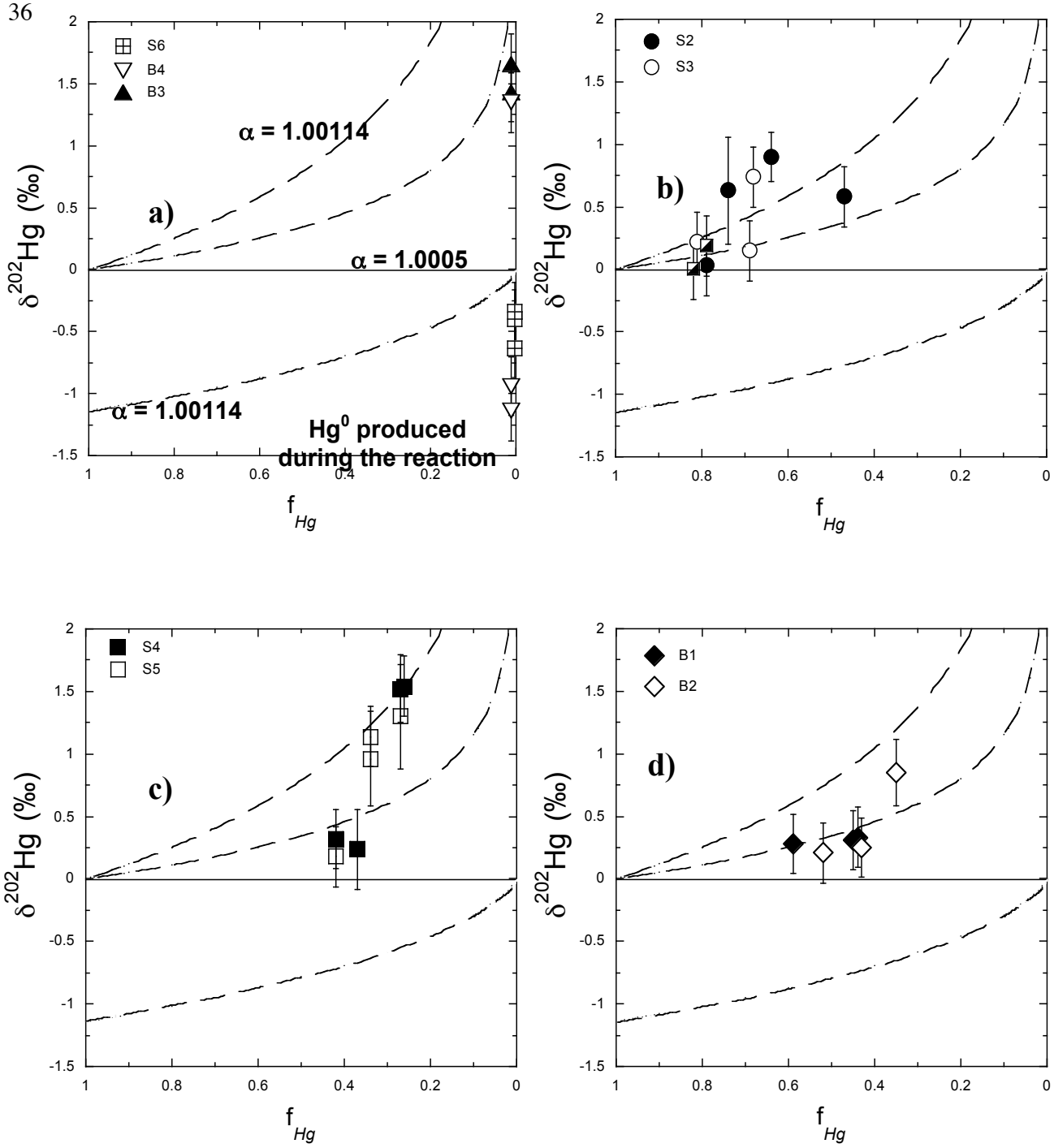

Table SI-S1: Concentrations and f_{Hg} for the Hg(II) fractions remaining in solution in function of the time for each experiment

Exp	S0		S1		S2		S3		S4		S5		S6		B1		B2		B3		B4
Time elapsed (sec)	Hg remaining (µg.ml^{-1})	f_{Hg}	Hg remaining (µg.ml^{-1})	f_{Hg}	Hg remaining (µg.ml^{-1})	f_{Hg}	Hg remaining (µg.ml^{-1})	f_{Hg}	Hg remaining (µg.ml^{-1})	f_{Hg}	Hg remaining (µg.ml^{-1})	f_{Hg}	Hg remaining (µg.ml^{-1})	f_{Hg}	Hg remaining (µg.ml^{-1})	f_{Hg}	Hg remaining (µg.ml^{-1})	f_{Hg}	Hg remaining (µg.ml^{-1})	f_{Hg}	Hg remaining (µg.ml^{-1})
0	19.9	1.00	19.9	1.000	19.9	1.000	19.9	1.000	19.9	1.000	19.9	.000	19.9	1.000	19.9	1.000	19.9	1.000	19.9	1.000	19.9
120	17.6	0.89	15.8	0.794	15.8	0.794	16.1	0.809	7.7	0.386	8.2	0.412	0.056	0.003	10.1	0.508	11.8	0.593	0.158	0.008	0.12
240	18.4	0.90	15.3	0.769	15.5	0.779	15.7	0.789	7.5	0.377	8.7	0.437	0.06	0.003							
360	16.6	0.88	15.3	0.769	14.6	0.734	16.4	0.824	8.5	0.427	8.1	0.407	0.05	0.003							
480	16.9	0.85	15.9	0.799	14.3	0.719	16.2	0.814	7.0	0.353	6.2	0.312	0.057	0.003							
600	17.0	0.85	15.8	0.794	13.2	0.663	15.6	0.784	7.7	0.387	5.9	0.296	0.058	0.003	9.4	0.470	10.7	0.539	0.132	0.007	0.10
900	16.9	0.85	15.8	0.794	12.8	0.643	13.5	0.678	3.5	0.177	6.0	0.299	0.057	0.003							
1200															7.1	0.357	8.7	0.437	0.121	0.006	0.11
1320	16.7	0.84	15.7	0.789	14.8	0.744	15.2	0.764	5.9	0.296	7.6	0.382	0.058	0.003							
1800	17.0	0.85	14.5	0.729	9.4	0.472	13.7	0.688	4.5	0.224	5.1	0.257	0.047	0.002							
2400															7.9	0.398	9.3	0.466	0.117	0.006	0.13
3600															8.6	0.432	8.9	0.447	0.154	0.008	0.03

39

Table SI-S2: Isotopic composition (δ^{202}Hg) of Hg(II) fractions remaining in solution

Exp	GR2 (mM)	Time elapsed (Sec)	f_{Hg}	n[a)]	δ^{202}Hg (‰)	2SE
S0	0.00	120	0.89	2	0.00	0.25
		900	0.85	2	0.07	*0.24*
		1800	0.85	2	0.14	*0.24*
S1	0.01	120	0.82	2	0.00	*0.24*
		1800	0.79	2	0.19	*0.24*
S2	0.06	120	0.79	2	0.03	*0.24*
		900	0.64	3	0.85	*0.24*
		1320	0.74	3	0.63	0.43
		1800	0.47	2	0.58	*0.24*
S3	0.05	120	0.81	2	0.22	*0.24*
		900	0.68	2	0.74	*0.24*
		1800	0.69	2	0.15	*0.24*
S4	0.50	120	0.42	2	0.32	*0.24*
		480	0.37	2	0.24	0.32
		900	0.27	2	1.52	0.27
		1800	0.26	2	1.54	*0.24*
S5	0.50	120	0.42	2	0.18	*0.24*
		480	0.27	2	1.30	0.42
		900	0.34	3	0.96	0.38
		1800	0.34	3	1.14	*0.24*
S6	1.30	120	0.003	1	-0.63	*0.24*
		600	0.003	1	-0.34	*0.24*
		1800	0.002	2	-0.40	*0.24*
B1	0.88	120.0	0.52	2	0.21	*0.24*
		1200	0.35	2	0.85	0.27
		3600	0.43	2	0.25	*0.24*
B2	1.08	120.0	0.59	2	0.28	*0.24*
		1200	0.44	2	0.33	*0.24*
		3600	0.45	2	0.31	*0.24*
B3	1.42	120.0	0.01	1	-0.94	*0.24*
		1200	0.01	1	1.35	*0.24*
		3600	0.01	1	-1.14	*0.24*
B4	3.27	120	0.01	1	1.43	*0.24*
		1200	0.01	1	1.66	*0.24*

40 a) number of measurements